Expansion signatures in 35 H II regions traced by SOFIA [C II] emission

Faerber, T.; Anderson, L.D.; Luisi, M.; Bonne, L.; Schneider, N.; Ossenkopf-Okada, V.; ... ; Röllig, M.

The Astrophysical Journal, 990:30 (22pp), 2025 September 1 https://doi.org/10.3847/1538-4357/ade852

Expansion Signatures in 35 H II Regions Traced by SOFIA [C II] Emission

T. Faerber[1], L. D. Anderson[1], M. Luisi[1,2], L. Bonne[3], N. Schneider[4], V. Ossenkopf-Okada[4], A. G. G. M. Tielens[5,6], R. Simon[4], and M. Röllig[7,8]
[1] Center for Gravitational Waves and Cosmology, West Virginia University, Chestnut Ridge Research Building, Morgantown, WV 26505, USA
[2] Department of Physics, Westminster College, New Wilmington, PA 16172, USA
[3] Stratospheric Observatory for Infrared Astronomy, Universities Space Research Association, NASA Ames Research Center, MS 232-11, Moffett Field, CA 94035, USA
[4] I. Physikalisches Institut, Universität zu Köln, Zülpicher Str. 77, 50937 Köln, Germany
[5] Leiden Observatory, Leiden University, Niels Bohrweg 2, 2333 CA Leiden, The Netherlands
[6] Department of Astronomy, University of Maryland, College Park, MD 20742, USA
[7] Physikalischer Verein—Gesellschaft für Bildung und Wissenschaft, Frankfurt am Main, Germany
[8] Institut für Angewandte Physik, Goethe-Universität Frankfurt, Frankfurt am Main, Germany
Received 2025 April 8; revised 2025 June 9; accepted 2025 June 10; published 2025 August 22

Abstract

We analyze the expansion signatures of 35 H II regions mapped in [C II] 158 μm emission by the Stratospheric Observatory for Infrared Astronomy. The [C II] emission primarily traces photodissociation regions (PDRs) at the transition between ionized and neutral gas. The brightness and narrow line width of [C II] allow us to measure PDR expansion. Bubble-shaped regions often exhibit expansion, while irregular-shaped ones are less likely to. Of the 35 H II regions, 12 ($\sim$34%) exhibit clear expansion in position–velocity diagrams, making them expansion candidates (ECs), with an average expansion velocity of $\sim$12.2 km s^{-1}. The remaining 23 regions show no clear expansion signatures, though they may still be expanding below detection limits. Blueshifted expansion is more common (eight ECs solely blueshifted, one redshifted, three both), with mean velocities of $\sim$10.9 km s^{-1} (blueshifted) and $\sim$13.2 km s^{-1} (redshifted). A comparison of our observations to spherical expansion models supports expansion in eight of 12 ECs. Estimated dynamical ages are 10–100 times shorter than the ionizing star lifetimes, in agreement with the results of previous studies. Of the 35 regions, 14 ($\sim$40%) appear as [C II] bubbles; nine of the 12 ECs are bubble-shaped. Thermal pressure likely drives expansion in M43, while stellar winds dominate in M17, M42, RCW 120, and RCW 79. For other ECs, available data do not allow a definitive conclusion. Larger samples and more information about ionizing sources are needed to refine our understanding of H II region feedback and evolution.

Unified Astronomy Thesaurus concepts: H II regions (694); Interstellar medium (847); Stellar wind bubbles (1635); Star forming regions (1565)

1. Introduction

H II regions are ionized areas of the interstellar medium (ISM) surrounding high-mass OB-type stars. They occur when dense clouds of cold, neutral molecular/atomic gas become ionized by strong ultraviolet (UV) radiation from young OB stars that reside within them (B. Strömgren 1939). The prevalence, brightness, and angular size of H II regions makes them natural laboratories for detailed studies of the impact of high-mass stars, such as triggered star formation and cloud disruption.

Because of their simple geometry, studies of H II region expansion and triggered star formation have largely focused on so-called "bubble" H II regions. Approximately half of all identified H II regions can be classified as bubbles based on their mid-infrared (MIR; 5–40 μm) morphology, appearing annular or ring-shaped on a 2D map (E. Churchwell et al. 2006; L. Deharveng & A. Zavagno 2010; L. Anderson et al. 2012). We assume that the ring-like shape seen in a 2D projection of 3D real space is also homogeneous along the third spatial axis along the line-of-sight in at least one direction, resulting in a semispherical or spherical shell. Such a shell has been observed in the Cygnus region, referred to as the "Diamond Ring," which is assumed to represent a final stage of an expanding [C II] bubble (S. Dannhauer et al. 2025, in preparation).

This ring-like structure is generally observed in the transition region between the ionized gas of the H II region and the predominantly molecular gas beyond it called the photodissociation region (PDR). Although PDRs lack significant ionized hydrogen, they do have ionized gas from atoms with ionization potentials $\leqslant$13.6 eV. The most common ion in PDRs is therefore ionized carbon ([C II]), as carbon has an ionization potential of 11.3 eV and is the fourth most abundant element.

As the distance from the ionizing source increases, photons with energies $\geqslant$11.3 eV are absorbed, resulting in a relatively thin ionized carbon shell. However, it is not the distance itself, but rather the column density of absorbing material that primarily determines the extent of absorption (A. Tielens & D. Hollenbach 1985; D. J. Hollenbach & A. Tielens 1999; M. G. Wolfire et al. 2022).

The [C II] ($^2P_{3/2}\rightarrow{}^2P_{1/2}$) emission line at 158 μm is a commonly used spectral line for probing the spatial and kinematic properties of H II regions (G. Stacey et al. 1991; L. Anderson et al. 2019; C. Pabst et al. 2020; M. Luisi et al. 2021; L. Bonne et al. 2022, 2023b). This line is one of the brightest emission lines in far-infrared spectra in the ISM, and is therefore a powerful tool for investigating PDR dynamics where ionized carbon is present among the neutral gas

(A. G. G. M. Tielens 2005). The choice of [C II] emission as a tracer for analyzing H II regions is driven by several factors. In addition to being a bright tracer of H II region PDRs, [C II] emission has a relatively long wavelength of $\sim$158 μm (A. G. G. M. Tielens 2005), allowing it to penetrate dense clouds of gas and dust that absorb radiation at shorter wavelengths, revealing regions of the ISM that may be otherwise hidden from our view. However, the [C II] line is optically thick in bright, dense PDRs (C. Guevara et al. 2020; S. Kabanovic et al. 2022) and therefore does not always trace the full extent of the PDR layer.

The use of heterodyne techniques at 158 μm (THz frequencies) enables spectral resolving powers of up to $R \approx 10^6$ (where $R = \frac{\nu}{\Delta\nu} = \frac{\Delta\lambda}{\lambda}$ is the spectral resolving power), corresponding to subkilometer per second velocity resolutions, which is crucial for detecting fine-scale velocity structures indicative of expansion within PDRs. In contrast, optical and MIR studies typically rely on slit-spectrum grating spectrometers with resolving powers between $R = 10^3$–10^5. While high-resolution systems such as TEXES (J. Lacy et al. 2002; Q.-F. Zhu et al. 2005) have enabled similar analyses in the MIR, such instrumentation is limited and rarely reaches the precision achievable in the radio regime. In the scope of this research, the [C II] line allows us to search for kinematic signatures of expansion in the PDRs of a sample of H II regions.

The physical expansion of H II regions as they interact with their surrounding medium can influence the structure of the nearby interstellar environment. This expansion, driven by radiation and stellar winds from central OB stars, can compress surrounding gas and shape molecular cloud morphology. In some cases, this process may lead to secondary star formation along the edges of the expanding region, a phenomenon often referred to as "triggered star formation." Proposed mechanisms include the "collect-and-collapse" scenario (B. G. Elmegreen & C. J. Lada 1977; R. Weaver et al. 1977; L. Lancaster et al. 2024) and radiatively driven implosion (RDI; F. Bertoldi 1989; B. Lefloch et al. 1997). Observational studies have debated the statistical significance of triggered star formation (M. Pomarès et al. 2009; L. Deharveng & A. Zavagno 2010; N. Schneider et al. 2012; J. Dale et al. 2015), although individual cases, such as G24.47+0.49 (A. Saha et al. 2024), W5 (J. Karr & P. Martin 2003) and RCW 120 (A. Zavagno et al. 2006), show evidence of multi-epoch or localized triggered star formation. RDI and collect-and-collapse can also operate simultaneously, as suggested by simulations of RCW 120 by S. Walch et al. (2015). However, the presence of young stars does not always imply triggering, as seen in the Rosette Nebula, where stellar clusters are not associated with local OB stars (L. Cambrésy et al. 2013).

The morphology of an H II region can influence whether or not signs of expansion are detectable in its PDR. If the region is homogeneous and has a bubble morphology, it is more likely for uniform expansion to be detected than if the region is irregular. Irregular expansion is likely due to inhomogeneities in the density of the medium surrounding the central ionizing star.

Observational evidence for the expansion of H II regions has accumulated over the past two decades, particularly through velocity differences between the ionized gas and surrounding PDRs. The dominant drivers of this expansion—thermal pressure from photoionized gas and mechanical input from stellar winds—remain under active investigation. In some cases, expansion appears consistent with classical models of pressure-driven expansion, while in others stellar wind feedback may be required to explain the observed kinematics. Observations with the Stratospheric Observatory for Infrared Astronomy (SOFIA) have proven especially effective in tracing PDR dynamics, revealing expansion signatures in a number of well-studied regions (C. Pabst et al. 2020; M. Luisi et al. 2021; M. Tiwari et al. 2021; H. Beuther et al. 2022; L. Bonne et al. 2022, 2023b).

Most prior studies, however, have focused on individual regions and apply a range of different analysis methods, making it difficult to assess broader trends or compare expansion mechanisms across different environments. In this work, we aim to address this gap by applying a uniform methodology to a large sample of H II regions observed in [C II]. A detailed comparison between our results and previous studies is presented in Section 6.1. The work done in this paper builds on the approach of M. Luisi et al. (2021), expanding it to a larger sample of 35 regions to establish statistics on the expansion of H II regions and explore the roles of thermal pressure and stellar wind pressure in driving any observed expansion.

2. H II Region Expansion

2.1. Thermal Expansion

The Strömgren radius, $R_{s,0}$, of an H II region is defined as the radius from an ionizing UV source at which ionization and recombination are balanced (B. Strömgren 1939). The initial stationary Strömgren radius of a "dust-free" H II region is given by Equation (1):

$$R_{s,0} = \left(\frac{3F^*}{4\pi n_0^2 \alpha_B}\right)^{1/3}, \quad (1)$$

where n_0 is the ambient density of the cold, neutral medium, F^* is the total number of ionizing UV photons per second coming from the hydrogen ionizing source (OB star), and $\alpha_B = 2.6 \times 10^{-13}$ cm^3 s^{-1} is the hydrogen recombination coefficient (to all levels above the ground level, assuming an electron temperature of $T_e \approx 10^4$ K). If we take the range of F^* to be from 1×10^{46}–7.5×10^{49} photons s^{-1} (the lower bound is typical for a B1 star, the upper bound is typical for an O3 star; F. Martins et al. 2005) and the range of ambient densities to be $n_0 = 100$–10^4 cm^{-3},[9] we find the theoretical range in $R_{s,0}$ to be from 0.01 pc to 6.17 pc.

Figure 1 presents a schematic diagram of an expanding H II region. The central ionizing source is depicted as a star at the center. Surrounding it is a region of ionized hydrogen (H II), shown as a dark blue circle, where ionized hydrogen is more prevalent than other ionized species. This H II region has an overpressure that drives a shock front into the surrounding molecular cloud, sweeping up gas into a dense shell. The inside of this shell is illuminated by far-UV (6–13.6 eV) radiation, creating a PDR boundary, shown as the outer light blue ring. As the distance from the ionizing source increases, UV photons with energies $E \geqslant 13.6$ eV are absorbed, but species like carbon, which has an ionization potential below 13.6 eV, can still be ionized. The small dark clouds along the outer edge of the PDR front represent sites where triggered star

[9] Star-forming regions do not have densities as low as 100 cm^{-3}. However, as we are concerned with expansion out of star-forming regions into surrounding giant molecular clouds (GMCs), we can use the density of GMCs, which can have densities as low as 100 cm^{-3} (B. T. Draine 2011).

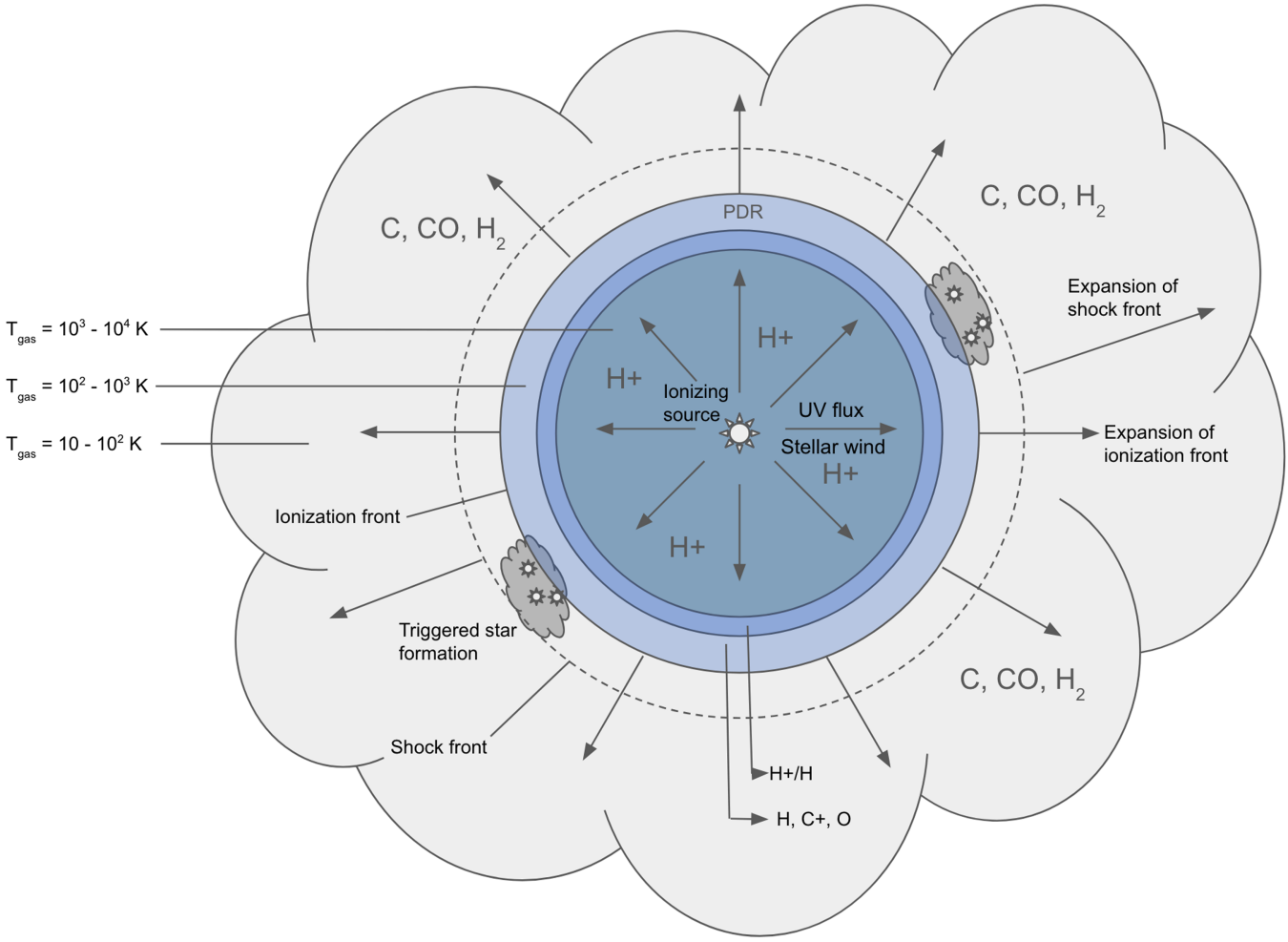

Figure 1. Schematic of the expanding ionization front of an H II region with triggered star formation at the edge of the expanding shell. This figure is not to scale, as the ionization front is very thin, about $\sim 10^{-3}$ pc, compared to the size of the H II region at $\sim$1 pc (A. C. Raga et al. 2012). In reality, the structure of an H II region is much more complex, with substructures in the region and a reverse shock front. For the purposes of this study, we stick with this simplified model of an H II region's structure to interpret our observations.

formation might occur as the PDR expands into the surrounding molecular cloud. A neutral shell is trapped between the ionization front and the shock front.

The time that it takes for an H II region to reach its initial Strömgren radius is given by the recombination timescale, $t_r = (\alpha_B * n_0)^{-1}$, where α_B is the "Case B" hydrogen recombination coefficient as in Equation (1) (L. Spitzer 1968).

As an H II region evolves, this Strömgren sphere expands beyond its initial Strömgren radius. This expansion is driven by increased thermal pressure of the ionized gas or the pressure of the hot plasma created by the stellar wind from the ionizing source(s). Initially, this expansion is faster than the sound speed in the ambient medium, causing a shock front that propagates either in front of, with, or eventually falls behind the ionization front (J. Franco et al. 2000).

An H II region's radius at time t due to thermal expansion as a function of its initial Strömgren radius is given by the relation from L. Spitzer (1968):

$$R_{\rm therm} = R_{s,0}\left(1 + \frac{7}{4}\frac{c_i t}{R_{s,0}}\right)^{4/7}, \quad (2)$$

where c_i is the sound speed in the warm, ionized medium (typically around $10\,{\rm km\,s^{-1}}$). $R_{\rm therm}$ represents the inner boundary of the PDR shell. If we differentiate Equation (2) with respect to t, we get the thermal expansion rate for an H II region:

$$\frac{dR_{\rm therm}}{dt} = v_{\rm therm} = c_i\left(1 + \frac{7}{4}\frac{c_i t}{R_{s,0}}\right)^{-3/7}. \quad (3)$$

In theory, as the H II region expands, its internal pressure drops as it nears the pressure of the surrounding medium, causing the shock wave to become subsonic and the expansion to stall (J. Franco et al. 1989).

If and when pressure equilibrium is eventually reached between the H II region and the surrounding molecular cloud, the expansion of the ionization front can stall at a stagnation radius given by the following relation from T. G. Bisbas et al. (2015):

$$R_{\rm stag} = R_{s,0}\left(\frac{2c_i}{c_o}\right)^{4/3}, \quad (4)$$

where c_o is the sound speed in the cold, neutral medium (typically around $0.3\,{\rm km\,s^{-1}}$.) Using sound speeds of $c_i \approx 10.5\,{\rm km\,s^{-1}}$ and $c_o \approx 0.3\,{\rm km\,s^{-1}}$, the theoretical range for $R_{\rm stag}$ is between 3.7 pc and 792.5 pc.

If we plug $R_{\rm stag}$ from Equation (4) into the expansion rate solution from L. Spitzer (1968) for $r(t)$ and solve for t, we get the time that it will take the expansion of an H II region to stagnate, $t_{\rm stag}$:

$$t_{\rm stag} = \frac{4}{7}\frac{R_{s,0}}{c_i}\left[\left(\frac{R_{\rm stag}}{R_{s,0}}\right)^{4/7} - 1\right]. \quad (5)$$

Using the ranges in $R_{s,0}$ and $R_{\rm stag}$ defined above, $t_{\rm stag}$ is seen to have a theoretical range from around 15,000 yr to 3 Myr. The OB stars powering H II regions have typical lifetimes of approximately 5–10 Myr, which is slightly longer on average than the theoretical range in stagnation times.

2.2. Stellar-wind-driven Expansion

Expansion in H II regions can also be driven by stellar winds from the ionizing source(s), generating cavities around massive stars called "wind-blown bubbles." R. Weaver et al. (1977) considers the interaction of strong stellar winds with the ISM in the early and intermediate stages of stellar evolution. The radius of the "cold shell," R_2, as defined in R. Weaver et al. (1977), is the radius of the outer shock front where the transition occurs between the hot and cold medium. This can be considered analogous to the outer edge of the PDR as defined by Equation (1), therefore we will refer to this radius as $R_{\rm wind}$. The evolution of $R_{\rm wind}$ over time is given as

$$R_{\rm wind} = \left(\frac{250}{308\pi}\right)^{1/5} L_w^{1/5}\rho_0^{-1/5}t^{3/5}, \quad (6)$$

where L_w is the mechanical luminosity of the stellar wind, ρ_0 is the density of the ambient medium, and t is time. Given a reasonable range of input parameters (molecular hydrogen with n = 100–10^4 cm^{-3}, t = 10^4 yr–10 Myr, $L_w = 10^{34}$–10^{37} erg s^{-1}), the theoretical range for $R_{\rm wind}$ ranges from 0.1 pc to 244.0 pc.[10] The expansion velocity of this interface over time is given by integrating Equation (6) with respect to t, giving

$$\frac{dR_{\rm wind}}{dt} = v_{\rm wind} = \left(\frac{250}{308\pi}\right)^{1/5}\frac{3}{5}L_w^{1/5}\rho_0^{-1/5}t^{-2/5}. \quad (7)$$

Using the same range for the input parameters shows that stellar wind can drive expansion with velocities of up to tens of kilometers per second, with a theoretical upper limit of $\sim$60 km s^{-1} (though expansion velocities this high have not been observed).

3. Data

SOFIA (decommissioned on 2022 September 29) was an airborne facility, representing a collaboration between NASA and the German Aerospace Center (DLR; A. Krabbe et al. 2013). The observatory was equipped with a suite of instruments including the German Receiver for Astronomy at Terahertz Frequencies (GREAT), which was used to conduct high-resolution spectroscopic observations (S. Heyminck et al. 2012). This was eventually replaced by upGREAT, an updated version of GREAT, during SOFIA Cycle 4 in 2016 (C. Risacher et al. 2018). upGREAT introduced mid-sized heterodyne arrays to GREAT, increasing its mapping speed by a factor of $\sim$10 (R. Güsten et al. 2007). The angular resolution for [C II] observations from SOFIA is 14.″1, while the velocity resolution is 0.04 km s^{-1} (raw) and 0.2 km s^{-1} (resampled for FEEDBACK sources; see below).

In this paper, we search for signs of expansion in all 35 H II regions observed by SOFIA in [C II] emission. We list the regions used in this study in Table 1 along with literature references (when previous literature for the source exists) and several notes about the sources and observations.

The 35 H II regions have a range of properties. Their ionizing sources range from single O stars (O9–O6), to small clusters ($\sim$10 O stars) to starburst regions. Four of the regions are located in the Large Magellanic Cloud or the Small Magellanic Cloud. These regions are N160, N44, N66, and N79. Of the 35 regions observed, 13 of them (Cygnus X, M16, M17, NGC 6334, NGC 6334IV, NGC 6334V, NGC 7538, RCW 120, RCW 36, RCW 49, RCW 79, W40, and W43) were observed as part of the FEEDBACK project (N. Schneider et al. 2020). The FEEDBACK project is a SOFIA Legacy Program aimed at understanding how massive stars interact with their environment by mapping [C II] and [O I] emission in Galactic H II regions to study feedback-driven gas dynamics. Details of the FEEDBACK observations are presented in N. Schneider et al. (2020).

All but seven of the 35 H II regions have distance estimates in the literature. For the seven that do not (G081+036, G083+936, G287+814, G301+138, G316+796, G317+426, and G320+088), we estimate distances using a Monte Carlo kinematic distance method from T. V. Wenger et al. (2018), using the Galactic rotation curve from M. Reid et al. (2014). This method takes the known Galactic longitude, latitude, and observed velocity of each source and compares the observed velocity to the expected velocity at different distances along the line of sight, as predicted by the Galactic rotation model. Since the parameters of the Galactic rotation curve and the observed velocity have uncertainties, the Monte Carlo method generates many random variations (resamples) of these parameters within their uncertainty ranges, producing a large set of possible distances. Each set of resampled values yields a new distance estimate, and after many iterations, a probability distribution of distances is built. For sources within the inner Galaxy, where two possible distances (near and far) can result from the same velocity, the most probable distance is determined by analyzing the distribution of all calculated distances and selecting the peak value, with uncertainties defined by the range of distances around this peak.

4. Methods

This study uses both position–velocity (PV) diagrams and velocity residual maps to search for expansion signatures in the [C II] data. A PV diagram is a 2D plot showing the intensity of spectral line emission as a function of spatial position and velocity along a chosen path. These paths are defined with start and end points on the moment-0 map of the H II region, and are therefore perpendicular to the line of sight.

One signature of expansion in a PV diagram is a semi-ellipse with the end points of the semiminor axis representing the systemic velocity. For uniform expansion, the PV diagram will resemble a full ellipse. For those H II regions where an expansion signature is observed, we define a semi-ellipse by

[10] We use the range of L_w values found in the literature from (L. Ellerbroek et al. (2013) and A. L. Rosen et al. (2014), which represent minima and maxima for the sample of H II regions in this study.

Table 1
Information for 35 H II Regions Observed by SOFIA in [C II] Emission

Region	R.A.	Decl.	SOFIA Map Size ($n \times m$)	H II Region Radius (arcsec)	Distance (kpc)	$\log(F^*)$	Bubble?	Literature
Cygnus	$20^h38^m30^s$	$42^d13^m00^s$	2505 × 2695	480.7	∼1.5[a]	49.58	No	N. Schneider et al. (2023), L. Bonne et al. (2023a)
G082+036	$20^h32^m21^s$	$43^d41^m14\overset{s}{.}8$	930 × 660	376.8	3.49(+0.96/ −0.91)[b]	⋯	No	⋯
G083+936	$20^h45^m38\overset{s}{.}9$	$44^d14^m52\overset{s}{.}3$	630 × 439	220.0	0.88 ± 0.02[b]	⋯	Yes	⋯
G287+814	$10^h45^m53\overset{s}{.}7$	$-59^d57^m05\overset{s}{.}1$	750 × 300	80.6	1.52(+0.37/ −0.96); 3.65 (+0.94/ −0.53)[b]	⋯	No	⋯
G301+138	$12^h35^m36^s$	$-63^d02^m33\overset{s}{.}2$	1200 × 600	54.8	3.29(+0.51/ −0.67); 5.64 (+0.39 / −0.75)[b]	⋯	Yes	⋯
G316+796	$14^h45^m19\overset{s}{.}7$	$-59^d49^m34\overset{s}{.}5$	675 × 540	311.8	2.43 ± 0.42; 9.66 ± 0.45[b]	⋯	Yes	⋯
G317+426	$14^h51^m36\overset{s}{.}5$	$-60^d00^m25\overset{s}{.}1$	585 × 300	71.7	14.53(+0.59/ −0.63)[b]	⋯	No	⋯
G320+088	$15^h14^m34\overset{s}{.}5$	$-58^d10^m35\overset{s}{.}9$	450 × 240	54.9	2.64(+0.48/ −0.19);10.30 (+0.20/ −0.57)[b]	⋯	No	⋯
M8	$18^h03^m46\overset{s}{.}6$	$-24^d22^m19\overset{s}{.}5$	255 × 300	429.8	1.25 ± 0.1[c]	48.63	No	M. Tiwari et al. (2019)
M16	$18^h18^m30^s$	$-13^d45^m00^s$	2295 × 2130	1124.4	2.10[d]	49.66	No	J. García-Rojas et al. (2006), R. L. Karim et al. (2023)
M17	$18^h20^m43\overset{s}{.}8$	$-16^d09^m41\overset{s}{.}5$	1050 × 570	1200.0	1.98[e]	49.77	Yes	M. S. Povich et al. (2007), W. Lim et al. (2020), C. Guevara et al. (2020)
M20	$18^h02^m29\overset{s}{.}3$	$-23^d01^m27\overset{s}{.}9$	525 × 480	550.4	1.67[f]	48.80	No	J. García-Rojas et al. (2006)
M42	$05^h34^m40\overset{s}{.}5$	$-05^d37^m51\overset{s}{.}9$	4050 × 2820	1749.6	0.44[g]	48.63	Yes	C. Pabst et al. (2020)
M43	$05^h35^m30\overset{s}{.}0$	$-05^d17^m00\overset{s}{.}0$	675 × 570	200.0	0.44[h]	47.00	Yes	C. Pabst et al. (2020), C. Guevara et al. (2020)
Mon R2	$06^h07^m46\overset{s}{.}8$	$-06^d22^m57\overset{s}{.}1$	900 × 468	241.8	0.78(+0.40/ −0.37)[i]	48.96	No	S. Treviño-Morales et al. (2019)
N19	$18^h18^m29^s$	$-13^d40^m00^s$	509 × 645	500.0	2.10[j]	48.29	Yes	J.-L. Xu et al. (2019)
N160	$05^h39^m35^s$	$-69^d39^m00^s$	975 × 240	100.0	49.59 ± 0.54[k]	50.23	No	N. Martín-Hernández et al. (2008)
N44	$05^h22^m06^s$	$-67^d58^m00^s$	675 × 360	100.0	49.59 ± 0.54[l]	49.00	No	S. Barman et al. (2022)
N66	$00^h59^m00^s$	$-72^d10^m00^s$	1050 × 285	100.0	62.44 ± 0.47[m]	50.32	No	E. Geist et al. (2022)
N79	$04^h51^m54^s$	$-69^d23^m30^s$	540 × 180	100.0	49.59 ± 0.54[n]	49.00	No	B. B. Ochsendorf et al. (2017)
NESSIE-A	$16^h41^m08^s$	$-47^d07^m10\overset{s}{.}9$	720 × 480	109.0	3.10[o]	49.00	Yes	S. E. Ragan et al. (2014), J. M. Jackson et al. (2024)
NGC 1977	$05^h35^m30\overset{s}{.}0$	$-04^d46^m42\overset{s}{.}9$	2025 × 2520	540.0	0.44[p]	45.48	Yes	C. Pabst et al. (2020)
NGC 2074	$05^h39^m09^s$	$-69^d30^m28^s$	390 × 132	100.0	49.59 ± 0.54[q]	50.25	No	C. E. Fleener et al. (2009)
NGC 6334	$17^h20^m31\overset{s}{.}2$	$-35^d51^m37\overset{s}{.}8$	240 × 180	119.0	1.75[r]	48.76	No	J. M. Jackson & K. E. Kraemer (1999), P. Carral et al. (2002), D. Russeil et al. (2016)
NGC 6334IV	$17^h20^m17\overset{s}{.}7$	$-35^d54^m29\overset{s}{.}2$	210 × 240	131.5	1.75[s]	45.48	No	J. M. Jackson & K. E. Kraemer (1999), P. Carral et al. (2002), D. Russeil et al. (2016)
NGC 6334V	$17^h19^m57\overset{s}{.}3$	$-35^d57^m09\overset{s}{.}8$	240 × 180	119.0	1.75[t]	45.48	No	J. M. Jackson & K. E. Kraemer (1999), P. Carral et al. (2002), D. Russeil et al. (2016)
NGC 7538	$23^h13^m47\overset{s}{.}8$	$61^d30^m01\overset{s}{.}9$	2250 × 1040	573.9	2.65[u]	49.64	Yes	H. Beuther et al. (2022), M. Werner et al. (1979)
RCW 120	$17^h12^m22\overset{s}{.}2$	$-38^d26^m54\overset{s}{.}3$	1275 × 1002	500.1	1.70[v]	48.29	Yes	L. Anderson et al. (2010), A. Zavagno et al. (2010), M. Luisi et al. (2021)
RCW 36	$08^h59^m28\overset{s}{.}8$	$-43^d45^m28\overset{s}{.}7$	1470 × 560	810.0	1.09[w]	48.44	No	L. Bonne et al. (2022)
RCW 49	$10^h23^m50\overset{s}{.}7$	$-57^d45^m50^s$	2400 × 2100	1333.0	2.30[x]∼6–7[y]	49.48	No	B. Whitney et al. (2004), M. Tiwari et al. (2021)

Table 1
(Continued)

Region	R.A.	Decl.	SOFIA Map Size ($n \times m$)	H II Region Radius (arcsec)	Distance (kpc)	$\log(F^*)$	Bubble?	Literature
RCW 79	$13^h40^m27\overset{s}{.}7$	$-61^d40^m27\overset{s}{.}6$	1200 × 600	477.5	3.9[z]	49.78	Yes	A. Zavagno et al. (2006)
S235	$05^h41^m01\overset{s}{.}2$	$35^d51^m16^s$	750 × 1440	438.3	1.60[aa]	47.56	Yes	L. Anderson et al. (2019)
W40	$18^h31^m28\overset{s}{.}7$	$-02^d08^m22\overset{s}{.}3$	1380 × 1020	1206.9	0.50[bb]	48.18	Yes	T. Shimoikura et al. (2018)
W43	$18^h47^m30^s$	$-02^d00^m00^s$	129 × 2170	346.6	5.5[cc]	51.00	No	Q. N. Luong et al. (2011)
W51	$19^h23^m50^s$	$14^d30^m40\overset{s}{.}5$	252 × 144	16.6	1.70[dd]	51.00	No	W. Lim & J. M. De Buizer (2019)

Notes.
[a] K. Rygl et al. (2012).
[b] M. Reid et al. (2014), T. V. Wenger et al. (2018).
[c] F. Damiani et al. (2019), N. F. Tothill et al. (2008).
[d] B. McBreen et al. (1982).
[e] Y. Xu et al. (2011).
[f] B. T. Lynds & E. J. Oneil (1985).
[g] R. Jeffries (2007).
[h] R. Jeffries (2007).
[i] S. Treviño-Morales et al. (2019).
[j] B. McBreen et al. (1982).
[k] G. Pietrzyński et al. (2019).
[l] G. Pietrzyński et al. (2019).
[m] D. Graczyk et al. (2020).
[n] G. Pietrzyński et al. (2019).
[o] A. A. Goodman et al. (2014).
[p] R. Jeffries (2007).
[q] G. Pietrzyński et al. (2019).
[r] D. Russeil et al. (2016).
[s] D. Russeil et al. (2016).
[t] D. Russeil et al. (2016).
[u] L. Moscadelli & C. Goddi (2014).
[v] M. A. Kuhn et al. (2019).
[w] F. Damiani et al. (2019).
[x] T. Belloni & S. Mereghetti (1994).
[y] P. Benaglia et al. (2013).
[z] L. Bonne et al. (2023b).
[aa] L. Anderson et al. (2019).
[bb] F. Comerón et al. (2022).
[cc] T. Bania et al. (1997), D. S. Balser et al. (2001).
[dd] B.-C. Koo (1997).

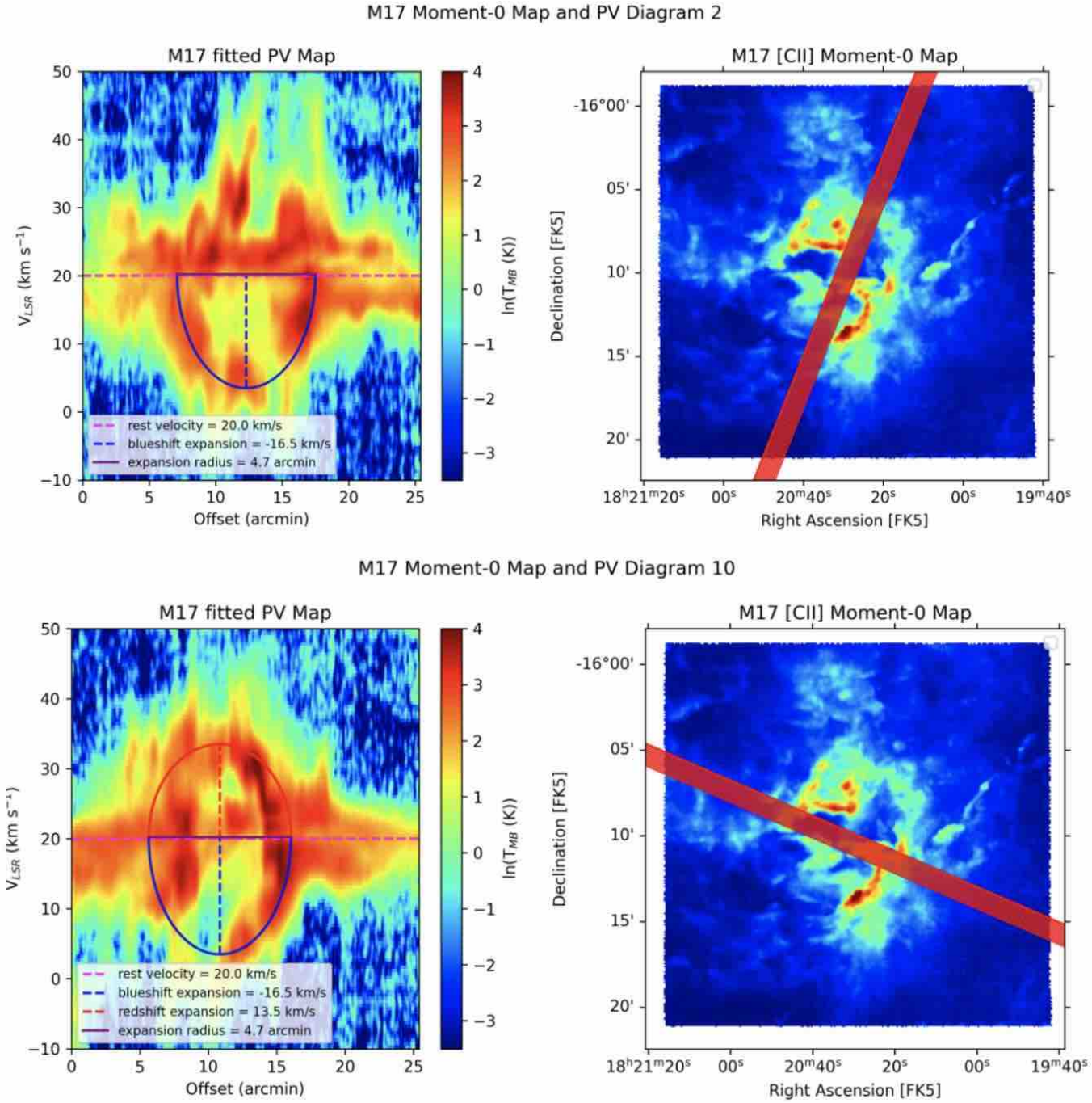

Figure 2. Two PV diagrams for M17. The left column shows the PV diagrams, and the right column shows moment-0 maps of the areas that the corresponding PV diagrams are extracted from. The *x*-axis in the first PV diagram represents distance from left to right along the red area in the moment-0 map. PV diagram 2 shows a blueshifted shell expanding at ~ -16.5 km s^{-1} with no redshifted counterpart. PV diagram 10 displays redshifted and blueshifted shells, expanding at ~ 13.5 km s^{-1} and ~ -16.5 km s^{-1}, respectively.

eye that approximates the signature seen in the PV diagram (as in M. Luisi et al. 2021).

For each of the 35 regions in the study, we create 16 PV diagrams using paths at evenly spaced angles through the H II region centers. For 21 of the 35 H II regions, the center of the region is taken from the Wide-field Infrared Survey Explorer (WISE) catalog of Galactic H II regions (L. D. Anderson et al. 2014). For the remaining 14 regions (N79, N160, NESSIE-A, NESSIE-A sub-bubble, NGC 6334, NGC 1977, N44, N19, NGC 2074, G083+936, RCW 36, M17, N66, and M43) we define a center that better matches the [C II] emission. We define the path widths for each H II region to be large enough that the resultant PV diagrams have high signal-to-noise ratio (S/N) but are not so large as to mix signals from different areas of the maps. Figure 2 shows two of the 16 PV diagrams taken along different paths across the moment-0 map of M17. The red areas overlaid on the moment-0 maps in the right panels show the region from which the PV diagram in the corresponding left panel is extracted. The PV *x*-axis, starting at zero, runs from the left to the right of the red area along its

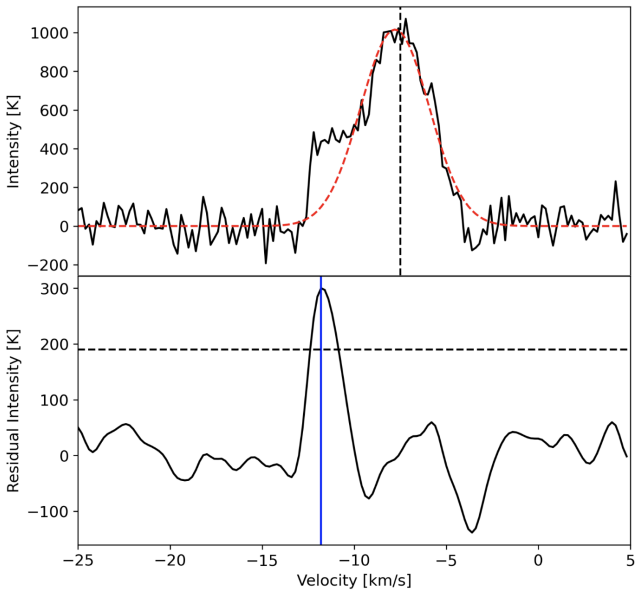

Figure 3. Example of the spectral subtraction process used to identify expansion signatures in RCW 120. The top panel shows the observed [C II] spectrum (black) extracted from a subcube, along with the fitted Gaussian (red dashed line) around the systemic velocity (vertical black dashed line). The bottom panel presents the residual spectrum after subtracting the fitted Gaussian, highlighting any remaining velocity components. A significant residual feature with a flux density greater than 3 times the rms noise at a blueshifted velocity relative to the systemic velocity (shown by the vertical solid blue line) is visible, indicating a possible expansion signature.

longest spatial axis (the shorter spatial axis is the one that is summed).

For regions with visual identification of expansion in at least one of the 16 PV diagrams, we produce velocity residual maps. For this analysis, we first generate an observed velocity map of the region, where we bin the data cube in R.A. and decl. into $n \times m$ subcubes (where the length and width of each subcube is the same). These subcubes are much larger than the beam size of SOFIA when observing at 158 μm, which is around 14″. We choose the size of the subcubes based on the similar analysis performed by M. Luisi et al. (2021), where subcube size is selected to maximize the S/N of the [C II] expansion signal. In each of these subcubes, we create an average [C II] spectrum of the observed emission and remove a fitted (using nonlinear least-squares optimization) Gaussian at the systemic velocity by subtracting it from the observed spectrum. The result is a rest-velocity subtracted spectrum where any residual peak in intensity could represent other velocity components in the subcube, such as expansion signatures. Figure 3 shows this process carried out on a spectrum from one of the subcubes in RCW 120 containing an expansion signal. For blueshifted expansion we search for residual velocity components less than the subtracted systemic velocity, while for redshifted expansion we search for residual velocity components greater than the subtracted systemic velocity. We then generate a suite of predicted velocity maps for a uniformly expanding sphere with a range of expansion velocities and expansion centers. On a 2D map, redshifted and/or blueshifted expansion of a sphere, when observed separately, will have the largest absolute value (manifesting as the largest offset from the systemic velocity) toward the center of the sphere, decreasing toward the edges until reaching the systemic velocity.

Finally, we subtract the predicted from the observed velocity maps for all generated models and identify the model that provides the lowest overall mean of the absolute value of all residuals produced by the model. We display our method for RCW 120 in Figure 4, which shows that the model of blueshifted expansion that best fits the observations is one centered on the [C II] emission (shown as contours) with an expansion velocity of $\sim$16.5 km s^{-1}. M. Luisi et al. (2021) used the same method on an incomplete field of RCW 120 and found an expansion value of 14 km s^{-1}.

5. Results

5.1. Position–Velocity Diagrams

Of the 35 H II regions studied in this paper, 12 exhibit expansion in at least one of their PV diagrams ($\sim$34% of the sample). Figure 2 shows two axes for M17 that show expansion signals, with PV diagram 2 showing only a blueshifted signal, while PV diagram 10 shows both a redshifted and a blueshifted signal. Table 2 shows the global expansion parameters for these 12 expansion candidates (ECs), along with expansion velocity values from the literature (when available). Of the 12 ECs, only G316+796 displays solely redshifted expansion with no blueshifted signature, while eight display only blueshifted expansion with no redshifted signature, and three show both redshifted and blueshifted expansion. The average expansion rate for all 12 ECs is $\sim$12.2 km s^{-1}. The average blueshifted expansion velocity of the ECs is $\sim$10.9 km s^{-1}, while the average redshifted expansion velocity is $\sim$13.2 km s^{-1}. The average percent of PV axes showing an expansion signature for all 12 ECs is 63%. As is expected, all four of the ECs that display expansion in 100% of their PV diagrams appear as bubbles in [C II] emission (Table 2). Of the 12 ECs, nine of them are bubbles (75%). On average, 72% of the PV cuts display expansion in the nine ECs that have bubble morphologies. On the other hand, only 34% of the PV cuts in the nonbubble ECs display expansion. Of the entire sample of 35 H II regions, 14 are bubbles (40%; see Table 1).

5.2. Velocity Residual Maps

Table 3 shows the results of the velocity residual map analysis for eight of the 12 ECs where the emission has a bubble morphology, appearing annular in its [C II] moment-0 map, and either a radius on the sky of at least 2.′5 or a peak [C II] moment-0 intensity of at least 400 K km s^{-1} (G083 +936, G316+796, N19, and RCW 36 are too faint and/or compact). The second column, labeled "$n \times m$," gives the binning parameters used for the spatial axes (see Section 4). The $v_{\rm r,map}$ and $v_{\rm b,map}$ columns give the values for the expansion velocity of the best-fit model for redshifted and blueshifted shells, respectively. The associated errors for these values can be inferred from the standard deviation plot shown in the right panel of Figure 5. Using the determined velocity of expansion and the observed S/N, the standard deviation can be determined. These standard deviations can also be used to determine the size of the error bars for the x-axis in Figure 6. The $\langle v \rangle_{\rm r,PV}$ and $\langle v \rangle_{\rm b,PV}$ columns indicate the average expansion values (across 16 PV axes per region) from the PV diagram analysis outlined in Section 5.1 for comparison also for redshifted and blueshifted shells, respectively. PV axes that did not show signs of expansion are excluded from the average,

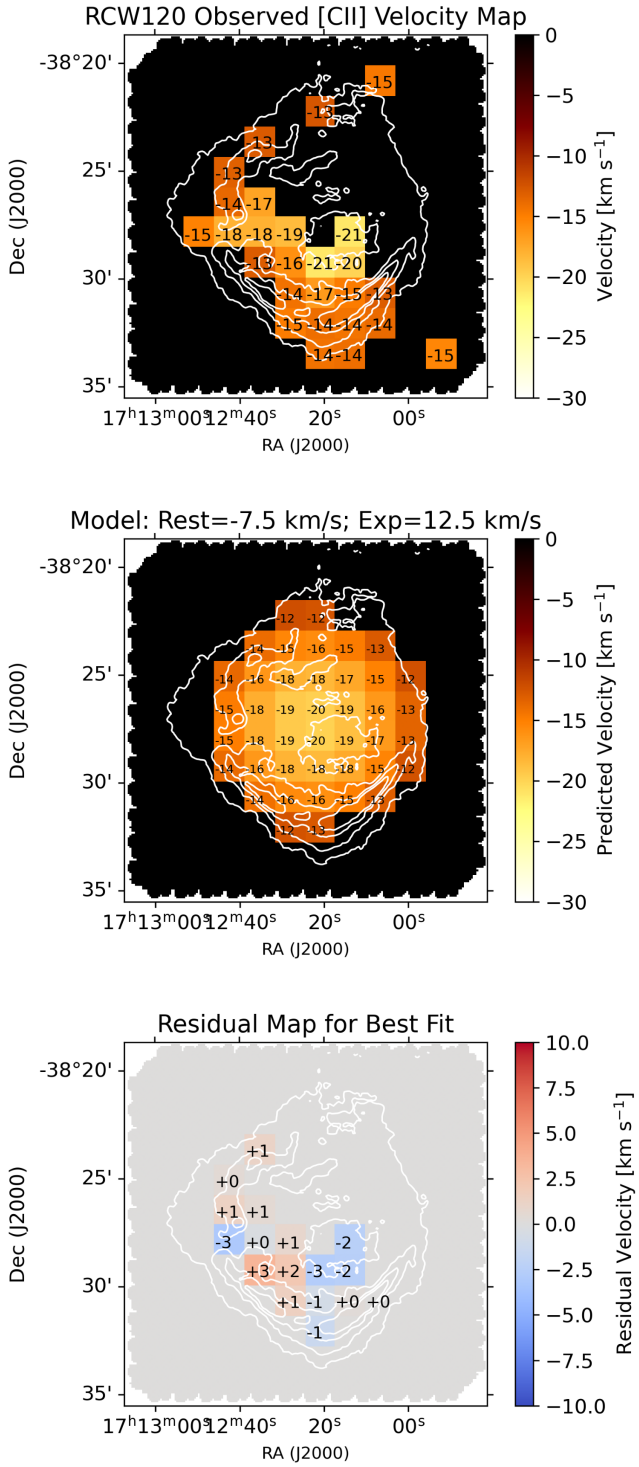

Figure 4. Velocity residual map analysis for RCW 120. Top: observed [C II] blueshifted velocity map for RCW 120, with expansion velocities in each subcube determined through the process outlined in Figure 3. Middle: predicted [C II] velocity map for specified systemic velocity, expansion velocity, center of expansion, and radius of expansion (systemic velocity and radius of expansion are defined as fixed parameters; expansion velocity and center of expansion are free parameters where a range of values is explored). Bottom: velocity residual map. The three subcubes with the largest magnitude of their residual are removed, as they change based on the region of the spectrum (minus the fitted rest Gaussian) that we search for a signal and cannot be fully trusted. For example, if we reduce the velocity cutoff from -10 km s^{-1} to -9 km s^{-1} the values in these subcubes for the observed map change from -11 km s^{-1} to -10 km s^{-1}.

which can lead to artificially inflated expansion values in regions where only a few axes exhibited expansion.

Only two of the 10 expansion signatures with associated errors in Table 3 fall within the error bars of their corresponding PV analyses, the redshifted expansion in RCW 79 and the blueshifted expansion for M43, suggesting one-to-one agreement of the two methods for these signals. The remaining nine signatures fall outside their PV-derived uncertainties, but still produced well-constrained expansion models based on the [C II] moment-0 morphology. The

Table 2
Expansion Candidate Global Parameters

Region	%[a]	Bubble?	Expansion Radius[b] (pc)	Expansion (lit) (km s^{-1})	Blueshift Expansion (km s^{-1})	Redshift Expansion (km s^{-1})	Blue Age (Myr)	Red Age (Myr)
G083+936	100	Y	(0.06, 0.15)0.09 ± 0.03	⋯	(−7.8, −9.3) −8.9 ± 0.5	(11.9, 13.4)12.6 ± 0.6	0.01 ± $\lesssim$ 0.01	0.01 ± $\lesssim$ 0.01
G316+796	50	Y	(1.84, 2.47)2.05 ± 0.23	⋯	⋯	(12.2, 13.4)13.0 ± 0.4	⋯	0.16 ± 0.02
M17	81	Y	(1.96, 2.88)2.50 ± 0.28	⋯	(−16.0, −19.5) − 17.5 ± 1.3	(13.0, 13.5)13.2 ± 0.2	0.14 ± 0.02	0.21 ± 0.01
M42	100	Y	(1.41, 2.14)1.68 ± 0.24	−13[c]	(−13.4, −14.0) − 13.8 ± 0.2	⋯	0.12 ± 0.02	⋯
M43	100	Y	(0.06, 0.23)0.13 ± 0.06	−6[d]	(−3.5, −4.0) − 3.6 ± 1.5	⋯	0.04 ± 0.01	⋯
N19	63	N	(2.75, 4.58) 3.91 ± 0.61	−4[e]	(−8.2, −8.8) − 8.3 ± 0.2	⋯	0.47 ± 0.08	⋯
NESSIE-Aa[f]	13	Y	(0.18, 0.18)0.18	⋯	(−16.4, −16.4) − 16.4	⋯	0.01	⋯
NGC 7538	44	Y	(1.31, 2.00)1.51 ± 0.25	∼−10[g]	(−11.1, −15.9) − 14.6 ± 1.6	⋯	0.11 ± 0.03	⋯
RCW 120	100	Y	(1.73, 2.97)2.17 ± 0.40	∼−15[h]	(−14.0, −16.0) − 15.3 ± 0.6	⋯	0.14 ± 0.03	⋯
RCW 36	19	N	(0.98, 1.21)1.10 ± 0.09	∼−5.2[i]	(−7.8, −9.0) − 8.5 ± 0.5	⋯	0.13 ± 0.01	⋯
RCW 79	63	Y	(7.94, 11.91)9.64 ± 1.16	$\leqslant$25[j]	(−8.5, −14.8) − 11.6 ± 2.6	(13.5, 14.7)14.1 ± 0.5	0.72 ± 0.07	0.85 ± 0.26
W40	19	N	(0.43, 0.55)0.50 ± 0.05	⋯	(−11.4, −12.3) − 12.0 ± 0.4	⋯	0.04 ± 0.01	⋯

Notes.
[a] The second column of Table 2 (titled "%") shows the percentage of PV cuts (out of 16 total for each region) that display an expansion signature. If the column says 100, then all 16 of the PV cuts display an expansion signature.
[b] For the columns titled "Expansion Radius," "Blueshift Expansion," and "Redshift Expansion," the values are given as such: (minimum value, maximum value) mean value ± standard deviation.
[c] C. Pabst et al. (2020).
[d] C. Pabst et al. (2020).
[e] R. Karmin (2025, in preparation).
[f] There are no associated errors on the parameters for NESSIE-Aa because there is only one PV diagram showing expansion. Therefore there is no standard deviation, which is how the errors were determined.
[g] H. Beuther et al. (2022).
[h] M. Luisi et al. (2021).
[i] L. Bonne et al. (2022).
[j] L. Bonne et al. (2023b).

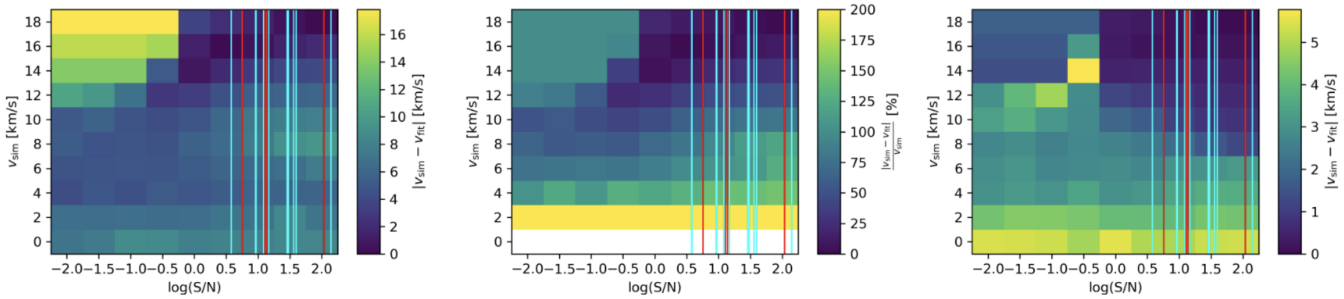

Figure 5. Parameter space for velocity residual map analysis simulations with simulated line width of 5 km s^{-1}. The y-axis shows the probed expansion velocity parameter space, while the x-axis shows the S/N parameter space in log-space. The vertical lines shown in both plots indicate the S/N of the observations with reliable fits from this analysis. The cyan lines represent the blueshifted signals, while the red lines represent the redshifted signals. Left: the color at each pixel in the left panel corresponds to the average absolute velocity offset over 100 iterations between the simulated expansion velocity and fitted expansion velocity for a simulated model with the corresponding expansion velocity and S/N. Center: the color at each pixel in the center panel corresponds to the offset between the simulated and fitted expansion velocities as a percentage of the simulated expansion velocity over 100 iterations. Right: the color at each pixel in the right panel corresponds to the standard deviation of the offset between the simulated and fitted expansion velocities over 100 iterations.

Table 3
Velocity Residual Map Results

Region	$n \times m$	Subcube Size (arcsec)	$v_{r,map}$ (km s^{-1})	$\langle v \rangle_{r,PV}$ (km s^{-1})	log(Red S/N)	$v_{b,map}$ (km s^{-1})	$\langle v \rangle_{b,PV}$ (km s^{-1})	log(Blue S/N)
M17	16 × 16	34.99	10.0 ± 0.8	13.2 ± 0.2	2.04	14.0 ± 0.4	17.5 ± 1.3	2.15
M42	16 × 23	133.13	⋯	⋯	⋯	12.0 ± 0.6	13.8 ± 0.2	1.56
M43	18 × 19	149.72	⋯	⋯	⋯	7.0 ± 2.5	3.6 ± 1.5	1.17
NESSIE-Aa	18 × 22	26.66	⋯	⋯	⋯	10.0 ± 1.1	16.4[a]	0.96
NGC 7538	16 × 16	24.37	⋯	⋯	⋯	11.0 ± 1.3	14.6 ± 1.6	0.43
RCW 120	16 × 16	83.53	⋯	⋯	⋯	12.5 ± 1.0	15.3 ± 0.6	0.51
RCW 79	16 × 16	22.50	14.5 ± 0.5	14.1 ± 0.5	1.14	18.0 ± 0.2	11.6 ± 2.6	1.08
W40	22 × 22	128.18	⋯	⋯	⋯	13.0 ± 0.5	12.0 ± 0.4	1.46

Note.
[a] No associated error because there is only one PV diagram showing expansion.

average expansion velocity from the 10 velocity residual map analyses is 12.8 km s^{-1}. Two maps model redshifted shells (M17 and RCW 79) with values of 10.0 km s^{-1} and 14.5 km s^{-1}, respectively. The remaining eight maps model blueshifted shells (M17, M42, M43, NESSIE-A, NGC 7538, RCW 120, RCW 79, and W40), with an average modeled blueshifted expansion velocity of 12.2 km s^{-1}. To test the robustness of this analysis, we repeat it on simulated data, as described in Section 6.6. Figure 6 shows the expansion velocity derived from our PV analysis on the y-axis versus the expansion velocity estimated from the velocity map on the x-axis. As indicated by the one-to-one line in Figure 6, the estimated expansion velocities for almost all regions fall within 5σ for the two approaches considered.

6. Discussion

6.1. Comparison with Previous Observations

Several previous studies have identified expansion signatures in H II regions, primarily based on velocity offsets between the ionized gas and surrounding PDRs. Our analysis builds on this body of work by providing a uniform comparison across a large sample.

D. A. Roshi et al. (2005) observed carbon recombination lines toward 18 ultracompact H II regions and identified dense PDRs in 11 sources. In nine cases, they found a consistent velocity offset of ∼3.3 km s^{-1} between the PDR and ionized gas, which they interpreted as evidence of expansion. M. Kirsanova et al. (2017) studied 14 regions in CS(2–1) and ^{13}CO(1–0), detecting a 1.2 km s^{-1} offset in G183.35−0.58, which they interpreted as expansion of the H II region into the molecular cloud. In follow-up work, M. S. Kirsanova et al. (2020) observed S235 in [C II], interpreting the velocity structure as further evidence of expansion.

Several studies using [C II] observations with SOFIA have reported expansion in individual H II regions. C. Pabst et al. (2020) reported expansion velocities of ∼13 km s^{-1} in M42, ∼6 km s^{-1} in M43, and ∼1 km s^{-1} in NGC 1977, concluding that stellar winds likely dominate the expansion in M42, while thermal pressure may drive expansion in M43 and NGC 1977. These observations have been extended in subsequent work by C. Pabst et al. (2022, 2024). M. Luisi et al. (2021) observed an expansion velocity of ∼15 km s^{-1} in RCW 120 and attributed the expansion to stellar winds. Prior work by A. Zavagno et al. (2006) suggested that the expansion of RCW 120 may be triggering star formation along the southwestern edge of the region. M. Tiwari et al. (2021) identified expansion in RCW 49 with a similar velocity (∼13 km s^{-1}), supported by evidence of stellar-wind-driven expansion from diffuse X-ray emission.

More recent SOFIA observations have reported expansion velocities of ∼5 km s^{-1} in RCW 36 (L. Bonne et al. 2022) and NGC 7538 (H. Beuther et al. 2022). L. Bonne et al. (2023a) observed simultaneous blueshifted and redshifted [C II] emission in RCW 79, identifying an expansion velocity of up to ∼25 km s^{-1}. This represents the first detection of both blueshifted and redshifted expansion signatures in the same

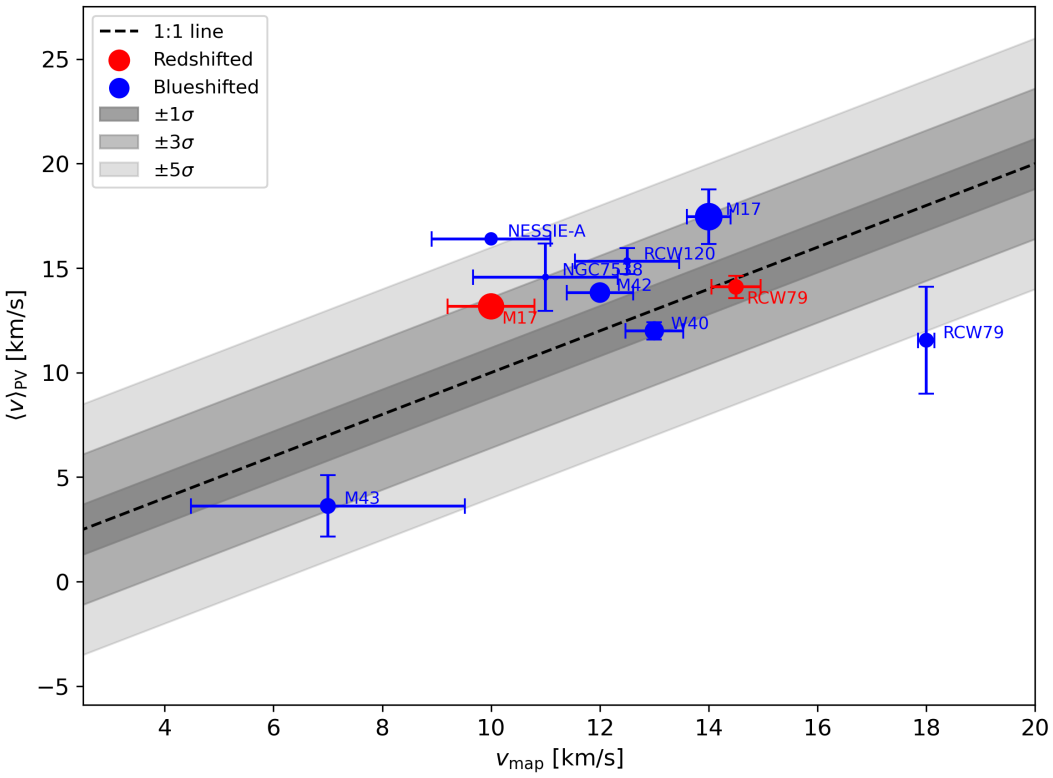

Figure 6. Comparison of estimated expansion velocities. The *y*-axis shows the expansion velocity determined through our PV analysis vs. the expansion velocity determined through our velocity map analysis on the *x*-axis. The *x*-axis errors are determined from the simulations producing the standard deviation plot in the right panel of Figure 5. The black dashed line represents a one-to-one ratio of the two expansion velocities, so that regions falling closer to this line represent those with better agreement between the PV and velocity map analyses. The gray shaded areas show where the observations are within 1, 3, and 5σ of the one-to-one line, where $\sigma = 1.2$ km s^{-1} is estimated as the standard deviation of the residuals between the PV and residual map velocities. The size of the filled circles scales as the size of the S/N of the observed signal, such that larger markers indicate an observation with a larger S/N and smaller markers indicate an observation with a smaller S/N. All values used to generate the plot can be found in Table 3.

region using [C II]. M. Figueira et al. (2017) suggested that expansion in RCW 79 may be responsible for triggering star formation at the interface between the H II region and the surrounding molecular material.

Finally, A. Saha et al. (2024) used the Atacama Large Millimeter/submillimeter Array and the Very Large Array to observe G24.47+0.49 in HCO^+(1–0) and radio continuum emission. They identified a 9 km s^{-1} expanding ring of HCO^+ surrounding the H II region and multiple collapsing dense cores along the expansion front, providing direct observational evidence of triggered star formation.

While these studies provide important context for understanding feedback-driven dynamics, they generally focus on individual regions. In contrast, our sample includes 35 H II regions analyzed using a consistent method, allowing us to examine expansion signatures statistically across a wide range of morphologies and evolutionary stages. In several cases our results corroborate previously measured expansion velocities (e.g., M42, M43, RCW 120, and RCW 79), while in others we provide new measurements for previously unstudied regions.

6.2. Blueshift-dominated Expansion

Blueshifted expansion is more common than redshifted expansion in our sample of 12 ECs. Of the 15 total expansion signatures, 11 are blueshifted and only four are redshifted. We test the statistical significance of this asymmetry using a binomial test under the null hypothesis that blueshifted and redshifted signatures occur with equal probability (50%). The resulting *p*-value of 0.081 indicates that this asymmetry is statistically significant at the 5% level. Selection bias may influence the observed asymmetry, though the sample size of 12 ECs is too small to determine meaningful population statistics. The FEEDBACK program primarily targets well-known regions of massive star formation, which may be more likely to be "blister" H II regions like Orion, with dense background molecular clouds. Such a geometry would make them easier to detect at optical wavelengths, but the molecular material would inhibit redshifted expansion.

6.3. Radial Expansion Asymmetry

Eight of the 12 ECs (∼67%) do not display signs of expansion along every axis sampled. Estimated expansion velocities along the 16 axes differ, which we interpret as expansion asymmetry. We show this radial expansion asymmetry in Figure 7, which defines the expansion velocities along 16 different axes in the region RCW 79 (left panel).

We choose RCW 79 as an example because it has the largest expansion asymmetry of any EC in the sample. The blueshifted expansion values of RCW 79 range from −8.5 km s^{-1} to −14.8 km s^{-1}. There are also six axes stretching from the northeast to the southwest of the region (where the material is likely denser and therefore the intensity of [C II] emission is

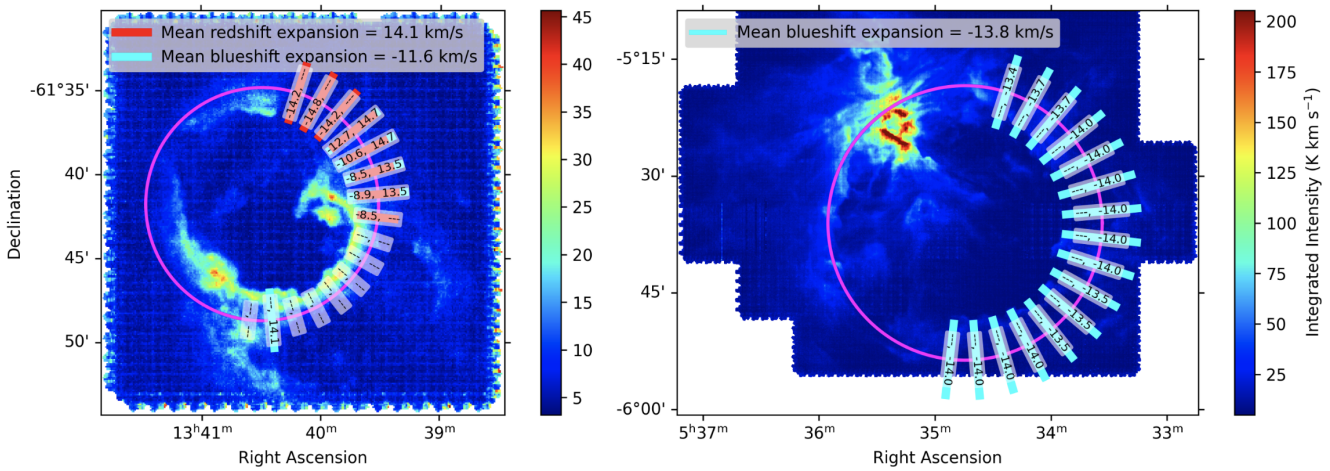

Figure 7. [C II] Moment-0 map of RCW 79 (left) and M42 (right) with expansion velocities listed for each axis of expansion. For RCW 79, the first listed velocity is the measured redshift along the corresponding axis, while the second listed number is the measured blueshift along the axis. The imaginary line connecting each pair of expansion velocity values to the center of the red circle corresponds to the axis (across the entire region) along which the aforementioned expansion velocities are observed. "- - -" represents no expansion seen along that axis of expansion. The red and cyan bars represent the relative magnitude of the observed redshifted and blueshifted expansion, respectively. RCW 79 and M42 are chosen to be compared as the blueshifted values for RCW 79 exhibit the most asymmetry of any EC in the sample, while for M42 they show the least.

higher, as a higher intensity of emitting radiation from ionized gas corresponds to a larger column density of the emitting species) that do not exhibit any detectable expansion. Our observations are consistent with a nonuniform density in the surrounding medium where the expansion is fastest and easiest to detect along axes pointing toward less dense surroundings. The right panel of Figure 7 shows the same plot for M42, where the expansion is found to be the most uniform of any EC in the sample ($-13.4\,\mathrm{km\,s^{-1}}$ to $-14.00\,\mathrm{km\,s^{-1}}$ with 100% of the PV diagrams showing blueshifted expansion signatures). It is possible that M42 displays a more uniform density in its surrounding medium, leading to a more uniform expansion than that seen in regions such as RCW 79.

6.4. Nonexpanding H II Regions

Of the 35 H II regions observed in this study, 23 do not exhibit any detectable signs of expansion in their [C II] PV diagrams. While this might initially suggest that these regions have reached pressure equilibrium, we tested this possibility by estimating their theoretical stagnation radii, R_{stag}.

For each of the 23 nonexpanding regions, we compiled values of the ionizing photon flux, F^*, from the literature and calculated R_{stag} following Equation (4). In all cases where F^* is available, we found that the radius of the H II region is smaller than its predicted stagnation radius by at least a factor of 10. This indicates that these regions have not yet reached pressure equilibrium with the surrounding ISM and are therefore not expected to have stagnated.

The lack of detected expansion signatures could be the result of several factors. First, expansion velocities may be too low to distinguish them from the systemic velocity given our spectral resolution. Second, expansion may be occurring asymmetrically or along lines of sight not probed by our PV diagrams. Finally, the surrounding environment may be too dense or clumpy to support a clearly defined expanding shell. Despite the absence of observable expansion features, the fact that these regions have not yet reached their stagnation radii suggests that they are likely still undergoing some expansion, potentially in a slow or highly nonuniform fashion.

6.5. Nonuniform Velocity Residual Maps

As can be seen in the bottom panel of Figure 4, we do not always attain a best-fit model with a velocity residual map where the residuals are all zero. Although RCW 120 shows expansion in all 16 of the axes probed with PV diagrams (see Table 2), the velocity residual map still shows some subcubes with larger residual values than others. The velocity residuals are larger in the northwest of the region, where M. Luisi et al. (2021) suggests that the bubble is bursting open into the surrounding ISM. This could point toward velocity components in the ionized gas along the line of sight that do not follow uniform expansion in the PDR. Such components could represent the erosion of molecular clouds as suggested by L. Bonne et al. (2023b). The column density of [C II] is also smaller in the center of the region than in the limb-brightened edges, which results in a smaller S/N in the center. This will result in a less robust extraction of the expansion signal, which could be influencing our residual map. For this reason, when defining our best-fit model using the sum of all residuals, we remove three of the subcubes from the observed map in Figure 4 near the center of the region, which give values highly dependent on the velocity used as a cutoff threshold to search for a residual expansion signal after rest Gaussian is subtracted.

6.6. Velocity Residual Map Analysis Robustness Test

To test the robustness of the results from our velocity residual map analysis carried out in Section 5.2, we rerun the velocity residual map analysis on simulated data with a range of S/Ns and expansion velocities. We allow the expansion velocity to vary from 0 to $18\mathrm{km\,s^{-1}}$ by steps of $2\,\mathrm{km\,s^{-1}}$, while we allow the S/N to range from -2 to 2 in log-space by steps of 0.5 using Equation (8) from D. D. Lenz & T. R. Ayres (1992):

$$\mathrm{S/N} = 0.7 \times \frac{T_L}{\mathrm{rms}}\left(\frac{\Delta V}{2.35}\right)^{1/2}, \tag{8}$$

Table 4
Comparison of Theoretical Radii and Expansion Velocities to Observed Radii and Expansion Velocities

Region	$\log(L_w)$	$R_{s,0}$ (pc)	$R_{\rm therm}$ (pc)	$R_{\rm wind}$ (pc)	$R_{\rm stag}$ (pc)	$R_{\rm PDR}$ (pc)	$v_{\rm therm}$ (km s^{-1})	$v_{\rm wind}$ (km s^{-1})	$\langle v_{\rm exp}\rangle$ (km s^{-1})
M17	37.00[a]	(0.26, 5.69)	(0.36, 13.22)	(0.39, 244.04)	(26.36, 567.92)	2.50	(1.70, 10.59)	(0.57, 57.03)	16.6
M42	35.90[b]	(0.11, 2.37)	(0.20, 8.37)	(0.23, 147.26)	(10.99, 236.75)	1.68	(1.17, 10.39)	(0.34, 34.41)	13.8
M43	⋯	(0.03, 0.68)	(0.10, 4.68)	⋯	(3.14, 67.76)	0.13	(0.69, 9.65)	⋯	3.6
NGC 7538	⋯	(0.11, 2.37)	(0.20, 8.37)	⋯	(10.99, 236.75)	0.18	(1.17, 10.39)	⋯	14.6
RCW 120	35.49[c]	(0.08, 1.83)	(0.17, 7.38)	(0.19, 121.64)	(8.46, 182.37)	2.17	(1.05, 10.29)	(0.28, 28.43)	15.3
RCW 36	34.00[d]	(0.10, 2.05)	(0.18, 7.80)	(0.10, 61.30)	(9.5, 204.62)	1.10	(1.10, 10.34)	(0.14, 14.33)	8.5
RCW 79	36.31[e]	(0.27, 5.73)	(0.36, 13.28)	(0.29, 177.57)	(26.56, 572.29)	10.26	(1.71, 10.59)	(0.42, 41.50)	12.5

Notes.
[a] A. L. Rosen et al. (2014).
[b] I. D. Howarth & R. K. Prinja (1989).
[c] M. Luisi et al. (2021).
[d] L. Ellerbroek et al. (2013).
[e] F. Martins et al. (2010).

where ΔV is the velocity resolution of the observations, around 0.5 km s^{-1}, T_L is the brightness of the expansion signal, and the rms is the spectral noise of the observation. The most possibly influential fixed parameter is the simulated line width for both the rest and expansion signal, which is set to 5 km s^{-1} for both. This line width is selected as it is characteristic of the observed emission lines in 12 ECs.

We run the simulation 100 times for each combination of the two free parameters. We show the average difference between the simulated and fitted expansion velocities for the explored free-parameter space in Figure 5. In this figure, the left panel shows the absolute difference between the simulated and fitted expansion velocities, while the right panel color bar shows the absolute difference as a percent of the simulated expansion velocity. We expect that when the S/N value of the expansion signal is higher and the simulated expansion velocity is higher (the upper-right corner of both graphs in Figure 5), our results will be more reliable and the pixels will have lower values in this area. This relationship is seen in both of the plots. The vertical lines shown in both plots indicate the S/N of the observations with reliable fits from this analysis. The cyan lines represent the blueshifted signals, while the red lines represent the redshifted signals. The observed S/N values are estimated as the average S/N of the redshifted/blueshifted expansion signal in the brightest 50% of subcubes within the radius defined in Section 4.

Table 3 summarizes the results of the velocity residual map fitting for each region with a successful fit and also shows the S/N for the observed expansion signals. Using the range in expansion velocities from this table along with the tabulated S/N values, we can look at Figure 5 and see that most of our observations fall in the upper-right corner of both plots with S/N values greater than $\log_{10}(0.5) = 3$ and a sample average expansion velocity of $\sim$12.2 km s^{-1}.

For the 23 regions without a detected expansion signal, it is likely that these nondetections could be due to a combination of three different factors. The expansion velocity could be so low (or zero, producing no expansion signal) that its expansion signal blends with the systemic velocity signal. How much this interferes with detecting the expansion signal will be a function of the line width (which we have set as a fixed parameter in the simulations) and the expansion velocity, since a smaller line width and larger expansion velocity will have a clearer expansion signal, while a wider line width and smaller expansion velocity will result in a blended rest and expansion signal. It is also possible that the expansion signal is low enough and/or the noise could be high enough that the S/N is not large enough to produce a clear expansion signal. Finally, a region with an irregular shape and nonuniform expansion will be harder to fit with the velocity residual map analysis than a region appearing as a bubble with uniform spherical expansion. It could be a combination of all three of these factors that results in no detection of expansion signals in 23 of the 35 regions in the sample ($\sim$66%).

6.7. PDR Radii and Dynamical Lifetimes

The observed PDR radii are shown in Table 4 along with stagnation radii and theoretical radii for both stellar-wind- and thermal-pressure-driven expansion. All of the observed PDR radii fall below the theoretical range for the stagnation times. It is therefore unlikely but not impossible that we observe effects of stagnation during the ionizing source's lifetime.

If we assume that each EC begins its lifetime with a PDR radius of zero and make the simplifying assumption that the expansion velocity of the PDR front remains uniformly spherical (such that the physical radius along the line of sight is the same as the radius tangent to the observer's line of sight on the sky) and constant throughout the lifetime of the H II region, we can work backwards to estimate an upper limit on the dynamical age, $t_{\rm dyn}$, for each EC. This is an upper limit because the expansion velocity that we observe now should theoretically be the slowest that the expansion has been during the lifetime of the region, starting its lifetime with its fastest expansion and eventually slowing to the current observed expansion velocity. Since expansion with respect to the systemic velocity of each H II region is studied with redshift and blueshift separately, we will also refer to the "red age" and "blue age" of each region, shown in the last two columns of Table 2. We estimated these using the following equation:

$$t_{\rm dyn} = \frac{r_{\rm exp}}{v_{\rm exp}}, \tag{9}$$

where $r_{\rm exp}$ is the expansion radius and $v_{\rm exp}$ is either the redshifted or blueshifted expansion velocity. The values for $\langle t_{\rm dyn}\rangle$ (the weighted average of redshifted expansion and blueshifted expansion for each region, where the weighting is

done by the percentage of PV diagrams that display an expansion signature; see Table 4) for the ECs range from 0.04 Myr to 0.85 Myr. This is significantly shorter than the 1–10 Myr main-sequence lifetime of the OB stars that power H II regions.

One possible explanation for the observed discrepancy between the lifetime of OB stars and the dynamical ages of the regions in our sample is a negative density gradient moving away from the central ionizing source with a nonhomogeneous angular density distribution, which could drive fast expansion into the surrounding, less dense medium as the H II region evolves (M. Zamora-Avilés et al. 2019). In addition, the dynamical age of an H II region begins when the region "bursts" out of the dense core in which the central ionizing star was born. This could be much later than when nuclear fusion is first ignited in the protostellar core, resulting in dynamical lifetimes much shorter than the age of the ionizing source. The low derived dynamical ages could also highlight a selection bias toward younger, brighter regions in the sample.

In addition to these factors, cloud ablation could also contribute to the large observed expansion velocities in some of the regions. As ionizing radiation erodes dense cloud surfaces, ablated material is accelerated outward, sometimes reaching velocities comparable to or exceeding the observed expansion speeds. This effect has been documented in studies such as L. Bonne et al. (2023b), which observed high-velocity [C II] emission in RCW 79 due to photoablation of molecular clouds and radiation-driven flows. This could explain the low dynamical time estimates, as the high-velocity gas is continuously replenished while flowing outward. Consequently, [C II] primarily traces the gas currently being expelled from the region rather than a sustained ionization front that has been expanding since the onset of the ionizing source's lifetime. Similar mechanisms may be at play in some of the regions in our sample, particularly those with strong local density gradients that result in asymmetric erosion and acceleration of material.

6.8. Thermal Expansion versus Wind-blown Bubbles

Table 4 shows an estimated theoretical range of values for $R_{s,0}$, $R_{\rm therm}$, $v_{\rm therm}$, $R_{\rm wind}$, and $v_{\rm wind}$, among other parameters. These values are estimated from Equations (1), (2), (3), (6), and (7), respectively. This table also shows the observed PDR radii ($R_{\rm PDR}$) for all ECs for which values of $R_{s,0}$ could be estimated. $R_{\rm PDR}$ roughly represents the observed center of the PDR shell, while $R_{\rm therm}$ represents the theoretical inner boundary and $R_{\rm wind}$ represents the theoretical outer boundary of the PDR shell. The values are presented as pairs separated by commas that represent the minima and maxima given a range in the input parameters ($\rho_0 = 3.35 \times 10^{-22}$–$3.35 \times 10^{-20}$ g cm^{-3}; a number density of 100–10^4 cm^{-3} multiplied by the mass of an H_2 molecule, $m_{H_2} = 3.35 * 10^{-24}$; $t = 10^4$ yr to 1 Myr, $L_w = 10^{34}$–10^{37} erg s^{-1}). For the ECs that we are able to estimate theoretical ranges for $v_{\rm therm}$ and/or $v_{\rm wind}$ for, we compare these ranges to the PV-diagram-derived expansion velocity in the region (see Section 5.1). It is worth noting that the theoretical maxima for $v_{\rm therm}$ correspond to the earliest stages of expansion, when the swept-up shell mass is still negligible, and thus is not directly applicable to the more evolved regions considered here. In this section, we will compare our observed PDR radii and derived expansion velocities to the theoretical ranges for stellar-wind-driven expansion and thermal-pressure-driven expansion in an attempt to determine the dominant mechanism of expansion in the region.

We compare observed expansion velocities and PDR radii to theoretical expectations from both thermal- and wind-driven models, using the ranges shown in Table 4. In general, regions with observed expansion velocities significantly exceeding the maximum theoretical $v_{\rm therm}$ are likely dominated by stellar winds, while those with velocities within the range of $v_{\rm therm}$ are more consistent with thermal-pressure-driven expansion.

In M17, M42, RCW 120, NGC 7538, and RCW 79, the observed expansion velocities exceed the maximum expected from thermal pressure but fall within the range predicted for stellar-wind-driven shells. This suggests that stellar winds are the dominant driver of expansion in these regions. Notably, M17 and M42 each show PDR radii and expansion velocities consistent with wind-driven expansion, aligning with prior studies (e.g., C. Pabst et al. 2020). RCW 120 and RCW 79 similarly display high expansion velocities and large PDR radii indicative of stellar wind influence (M. Luisi et al. 2021; L. Bonne et al. 2023b). In NGC 7538, the high expansion velocity also points to wind-driven dynamics, although the region exhibits complex internal substructure that may complicate the interpretation (H. Beuther et al. 2022).

By contrast, M43 shows a low expansion velocity consistent with thermal-pressure-driven expansion, and no reliable L_w estimate is available to test for wind influence. This aligns with prior work suggesting a thermally expanding shell (C. Pabst et al. 2020).

RCW 36 presents an intermediate case: both the observed radius and expansion velocity fall within the ranges predicted by both models. Spatially resolved studies reveal slower expansion in dense molecular structures and faster expansion in cavity regions, suggesting that the variation in expansion velocity is tied to density variations in the surrounding ISM (L. Bonne et al. 2022). This is consistent with the scenario proposed by L. Bonne et al. (2022), in which the star formed in a thin molecular sheet. Once the expanding bubble broke out of the sheet, the expansion proceeded more rapidly in the perpendicular direction, appearing stellar wind driven in all directions despite asymmetry in the velocity field. This may help explain discrepancies between the stellar age and the dynamical age inferred from expansion modeling.

Overall, most regions with high expansion velocities are consistent with stellar-wind-driven shells, while a smaller subset, such as M43, are better explained by thermal pressure. RCW 36 exemplifies a case where both mechanisms appear to play a role, varying spatially across the region. When studied at X-ray wavelengths, many of the rapidly expanding bubbles (such as M17, M42, RCW 36, RCW 79, and W40) reveal the presence of hot plasma generated by stellar wind shocks (L. K. Townsley et al. 2014, 2018, 2019).

6.9. Stagnation Time

In addition to observed and theoretical PDR radii, Table 4 also shows the estimated theoretical values for $R_{\rm stag}$ (column 4, from Equation (4)), and $t_{\rm stag}$ (column 7, from Equation (5)) for the ECs for which information is available on their ionizing sources. Comparing the theoretical $t_{\rm stag}$ value with the observationally derived $\langle t_{\rm dyn} \rangle$ value shows that the inferred dynamical time is, on average, 10% of the expected stagnation time. For all of these calculations, it is assumed that the

Table 5
Ionizing Sources and Timescales

Region	Ionizing Source(s)	F^* (photons s^{-1})	t_{source} (Myr)	t_{stag} (Myr)	$\langle v_{exp} \rangle$ (km s^{-1})	$\langle t_{dyn} \rangle$ (Myr)	$\frac{\langle t_{source} \rangle}{t_{dyn}}$
M17	O4V-O4V[a]	$10^{49.77}$	~2.5	3.81	16.60	0.15	16.67
M42	O7V[b]	$10^{48.63}$	~5	1.59	13.83	0.12	41.67
M43	B0.5V[c]	$10^{47.00}$	~10	0.46	3.62	0.04	250.00
NGC 7538	O7V[d]	$10^{48.63}$	~5	1.59	14.57	0.11	45.45
RCW 120	O8V[e]	$10^{48.29}$	~6	1.23	15.33	0.14	43.48
RCW 36	O8V-O9V[f]	$10^{48.44}$	~7	1.37	8.47	0.13	52.63
RCW 79	O3V-O5V[g]	$10^{49.78}$	~2.5	3.84	12.56	0.86	2.94

Notes.
[a] M. M. Hanson & P. S. Conti (1995).
[b] C. Pabst et al. (2020).
[c] C. Pabst et al. (2020).
[d] G. Sandell et al. (2020).
[e] Y. Georgelin & Y. Georgelin (1970).
[f] R. Verma et al. (1994).
[g] A. Zavagno et al. (2006).

ambient density is $n_0 = 100$ cm^{-3}, and the hot and cold medium sound speeds are taken to be $c_i = 10.74$ km s^{-1} and $c_o = 0.34$ km s^{-1}, respectively. Every EC shows signs of expansion in at least one of their PV cuts, suggesting that stagnation has not occurred in their PDRs.

6.10. Ionizing Source versus Expansion

Table 5 shows our ECs for which information about the ionizing source(s) is available in the literature. The spectral type and approximate main-sequence lifetime of the ionizing source are shown, along with the average observed expansion velocity and dynamical time. The last column shows that t_{dyn} is at least 1 order of magnitude smaller than the lifetime of the ionizing source for all ECs analyzed. If we instead use Equation (5) to estimate t_{dyn} by replacing R_{stag} with R_{PDR} (see Table 4), we find that the dynamical times decrease by about a factor of 10.

6.10.1. F^* and L_w versus Expansion Velocity

We examine whether the expansion velocities of the H II region PDR fronts correlate with either the ionizing UV flux (F^*) or the mechanical luminosity (L_w) of the central source(s).

For ionizing photon flux, we find no clear trend: Regions with high UV output, such as M17 and RCW 79, show a wide range of expansion velocities from approximately 13–17.5 km s^{-1}. Other regions with similar or slightly lower fluxes, like RCW 120 and M42, exhibit comparable expansion rates. This spread does not agree with the prediction of Equation (3) that the expansion rate should scale with ionizing flux due to increased thermal pressure.

Several regions with known ionizing fluxes show no detectable expansion. These are typically not bubble-shaped and fall near or below our estimated detection threshold of ~3 km s^{-1}. This suggests that morphology, orientation, and local environmental conditions influence whether we observe expansion. All regions with expansion signatures in 100% of their PV cuts appear as bubbles in [C II] emission, supporting the idea that symmetrical regions are more likely to exhibit clear expansion.

We also compare expansion velocity with mechanical luminosity (L_w) where available, and again find no consistent trend. M17, which has the highest L_w (~10^{37} erg s^{-1}), expands rapidly, but RCW 79, with a similar L_w, expands more slowly. Conversely, RCW 36 shows moderate expansion (~8–9 km s^{-1}) despite having one of the lowest mechanical luminosities in the sample (~10^{34-35} erg s^{-1}). These results indicate that while stellar winds may contribute to expansion, they do not dominate. Expansion velocity likely depends on a combination of factors, including UV flux, mechanical feedback, density structure, morphology, and projection effects.

6.10.2. Ionizing Source Lifetime versus Dynamical Ages

When comparing the expansion-derived dynamical ages of our ECs to the estimated main-sequence lifetimes of their ionizing sources, in every case the dynamical age falls well below the stellar lifetime—typically by at least an order of magnitude (and in some cases by a factor of 100 or more.) This aligns well with results from other studies where dynamical ages estimated from classical expansion models are consistently shorter than the actual lifespans of the stars driving the ionization.

This discrepancy in age reflects the limitations of idealized models that do not account for all mechanisms at play. Several factors can delay or suppress the observable expansion of an H II region, including confinement by dense natal material, time-variable ionizing flux (R. Galván-Madrid et al. 2011), or expansion into a clumpy medium. For example, the ionization front may remain trapped within the dense core for tens to hundreds of thousands of years before breaking out and driving large-scale expansion (E. Keto 2002). During this time, the star continues to age, but the region's expansion "clock" has not yet started. Once the front breaks out, the expansion begins rapidly, but the inferred dynamical age—based on the current radius and expansion velocity—only captures the post-breakout phase.

6.11. Individual Regions

In this section, we discuss the results for three of our ECs that have not yet been discussed in the literature.

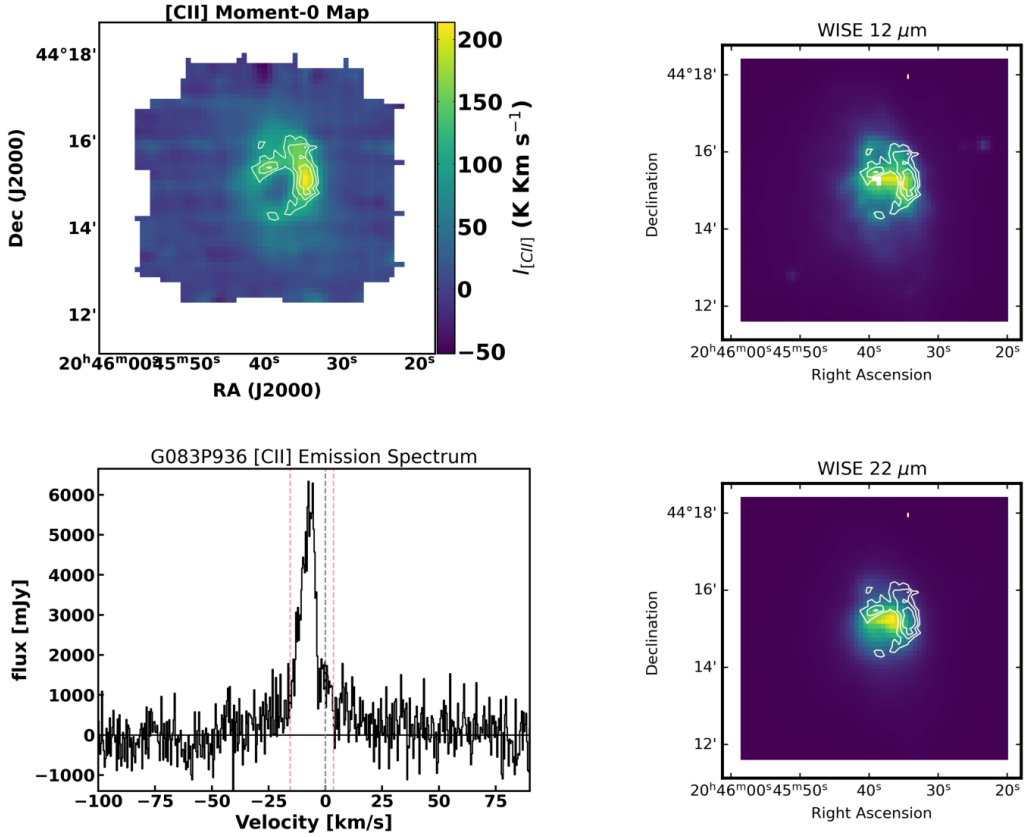

Figure 8. Top left: moment-0 map of SOFIA [C II] emission for H II region G083+936. Overlaid contours show 4, 5, 7, 9, 12, 15, and 18σ levels of detection for [C II] emission. Top right: WISE 12 μm emission with [C II] contours overlaid. Bottom left: SOFIA [C II] spectrum of entire field. Bottom right: WISE 22 μm emission with [C II] contours overlaid.

6.11.1. G083+936

H II region G083+936 appears as a compact bubble in [C II] emission with an opening in the southwest of its PDR, as shown in the upper-left panel of Figure 8. The PV analysis for this source shows that all 16 of the PV diagram axes explored display both redshifted and blueshifted expansion signatures. One of the PV diagrams for this regions is shown in Figure 9. This is the first H II region for which both redshifted and blueshifted expansion is present along all probed axes (see Table 5). The 0.09 ± 0.03 pc observed PDR radius of this source is the smallest in the sample (sample average $\sim$2.48 pc). The observed blueshifted expansion in the source is -8.86 ± 0.47 km s^{-1}, which is lower than the ~ -11.97 km s^{-1} sample average. The observed redshifted expansion in the source is 12.61 ± 0.57 km s^{-1}, which is also slightly lower than the $\sim$13.18 km s^{-1} sample average. The redshifted and blueshifted dynamical ages for the source are also the smallest in the sample. This together with the small observed PDR radius suggests that G083+936 may be relatively young and less evolved compared to the other H II regions in the sample.

6.11.2. G316+796

H II region G316+796 appears as a diffuse bubble in [C II] emission with openings in the northeast, east, and southwest of its PDR, as shown in the upper-left panel of Figure 10. The PV analysis for this source shows that eight of the 16 PV diagram axes explored display redshifted expansion signatures, while none display any blueshifted expansion signatures. The nondetection of blue- or redshifted emission in the PV diagrams of any region may therefore be a sensitivity limitation rather than definitive evidence of its absence. One of the PV diagrams for this regions is shown in Figure 11. The lack of a blueshifted counterpart suggests that the observed kinematics may be influenced by a line-of-sight orientation effect or an inherent asymmetry in the expansion process. The 2.05 ± 0.23 pc observed PDR radius of this source is slightly below the sample average of $\sim$2.48 pc. The observed redshifted expansion in the source is 12.95 ± 0.36 km s^{-1}, which is within range of the $\sim$13.18 km s^{-1} sample average. The dynamical ages for the source are also among the smallest in the sample. The redshifted dynamical age for the source is 0.16 ± 0.02 Myr, nearly in range of the average redshifted age in the sample of $\sim$0.21 Myr.

6.11.3. NESSIE-A Sub-bubble (NESSIE-Aa)

The H II region NESSIE-A appears as a long, wavy filament of ionized gas, as shown in the top-left panel of Figure 12. The filamentary portion of the region itself does not display signs of expansion; however, the sub-bubble in NESSIE-A (outlined by the red circle) exhibits distinct morphological and kinematic properties within the larger region. Denoted as NESSIE-Aa, the sub-bubble has a compact observed radius of 0.18 pc (the smallest in the sample of ECs) and displays exclusively blueshifted expansion with a velocity of -16.4 km s^{-1} in two of the 16 PV diagrams analyzed, shown in Figure 13. This

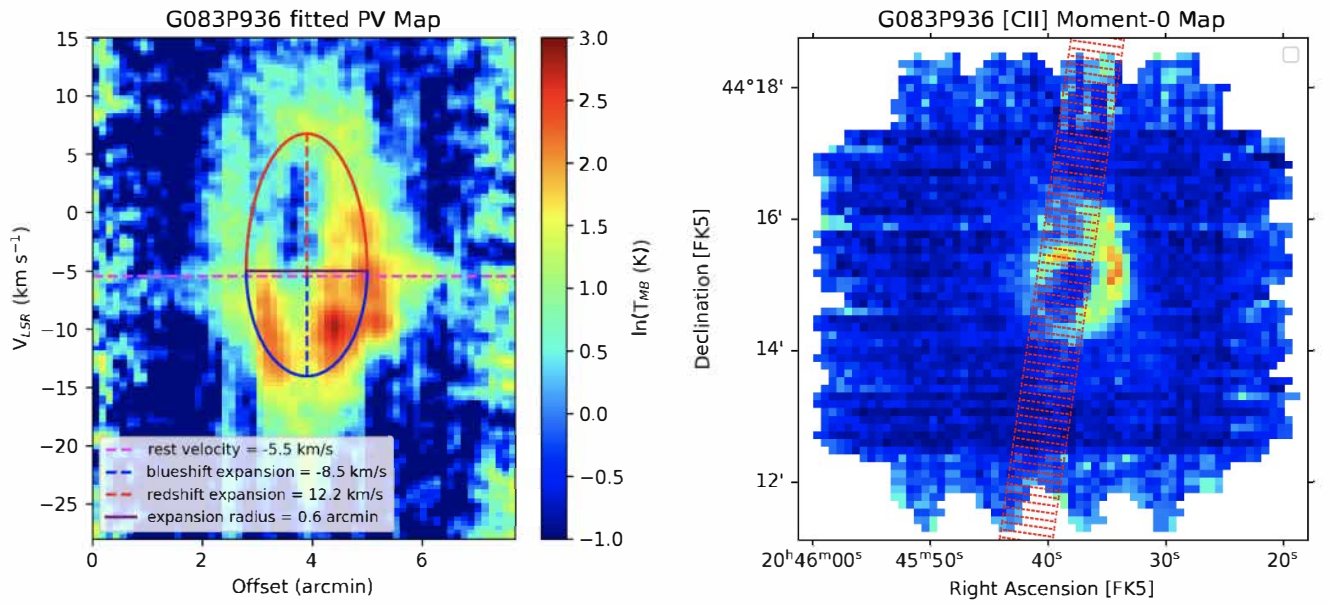

Figure 9. Left: PV diagram of G083+936. Right: [C II] moment-0 map of G083+936. The red area cutting across the field is the area from which the PV diagram on the left is derived.

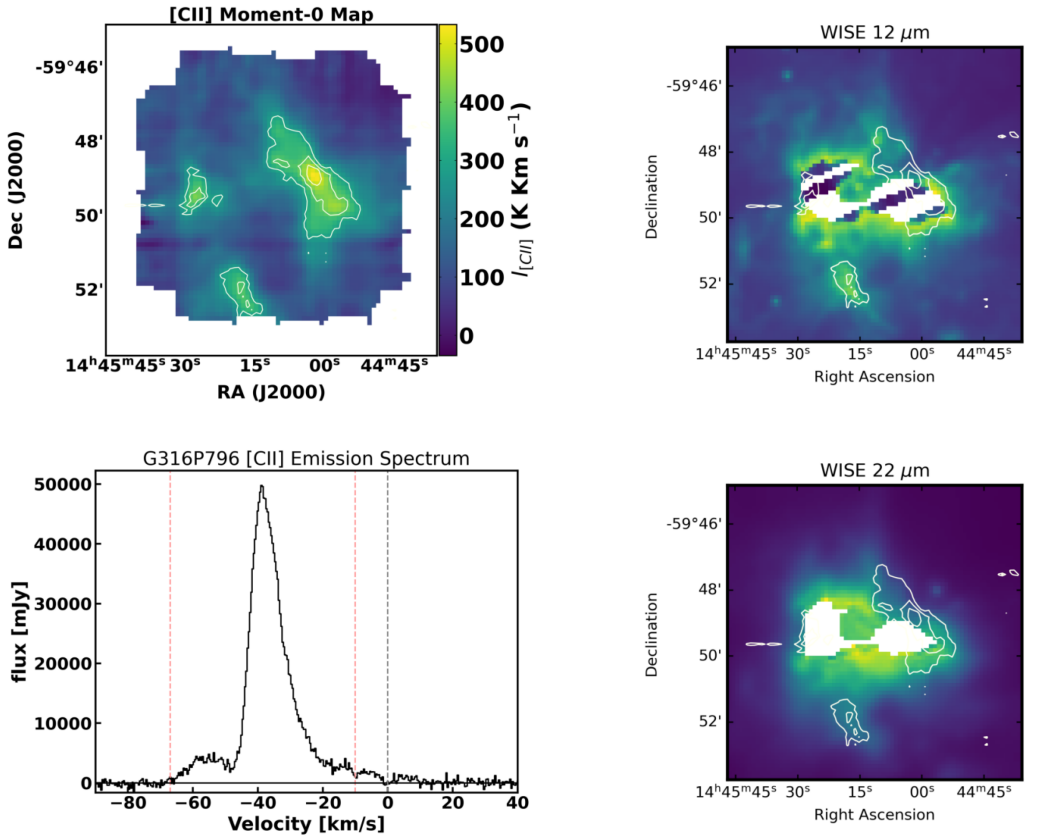

Figure 10. Top left: moment-0 map of SOFIA [C II] emission for H II region G316+796. Overlaid contours show 4, 5, 7, 9, 12, 15, and 18σ levels of detection for [C II] emission. Top right: WISE 12 μm emission (saturated) with [C II] contours overlaid. Bottom left: SOFIA [C II] spectrum of entire field. Bottom right: WISE 22 μm emission (saturated) with [C II] contours overlaid.

velocity is among the highest observed in the sample. The lack of a redshifted counterpart suggests that the observed kinematics may be influenced by a line-of-sight orientation effect or an inherent asymmetry in the expansion process. The compact size and high expansion velocity of NESSIE-Aa may indicate that the sub-bubble is in an early phase of evolution. The proximity

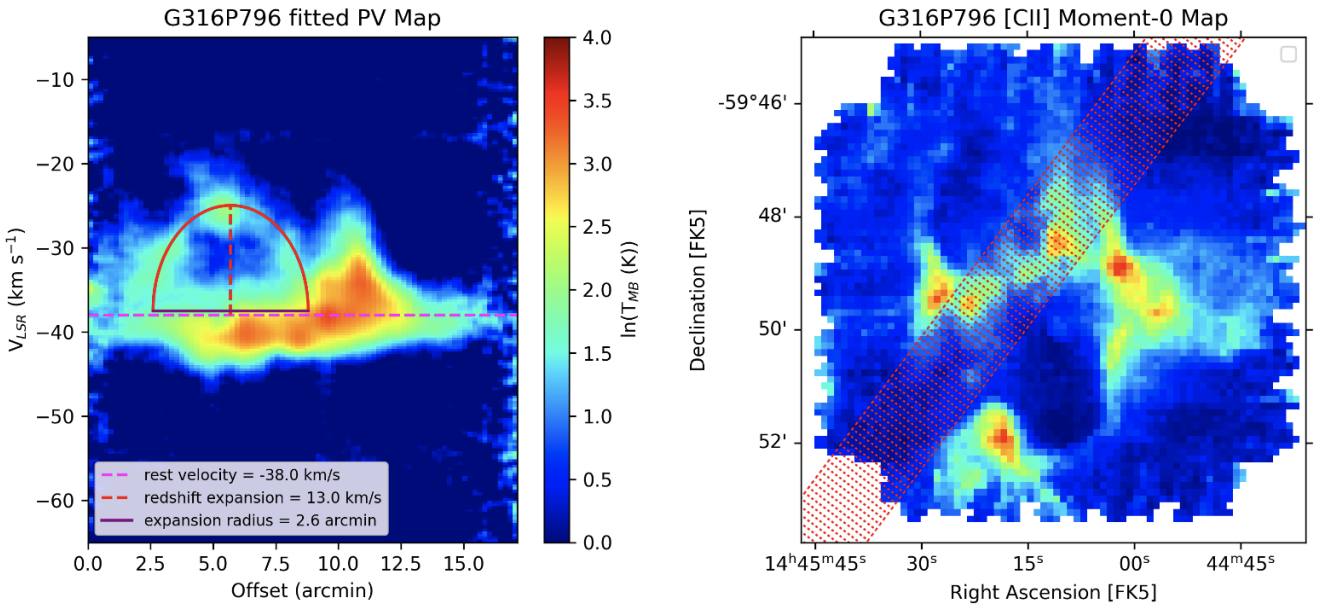

Figure 11. Left: PV diagram of G316+796. Right: [C II] moment-0 map of G316+796. The red area cutting across the field is the area from which the PV diagram on the left is derived.

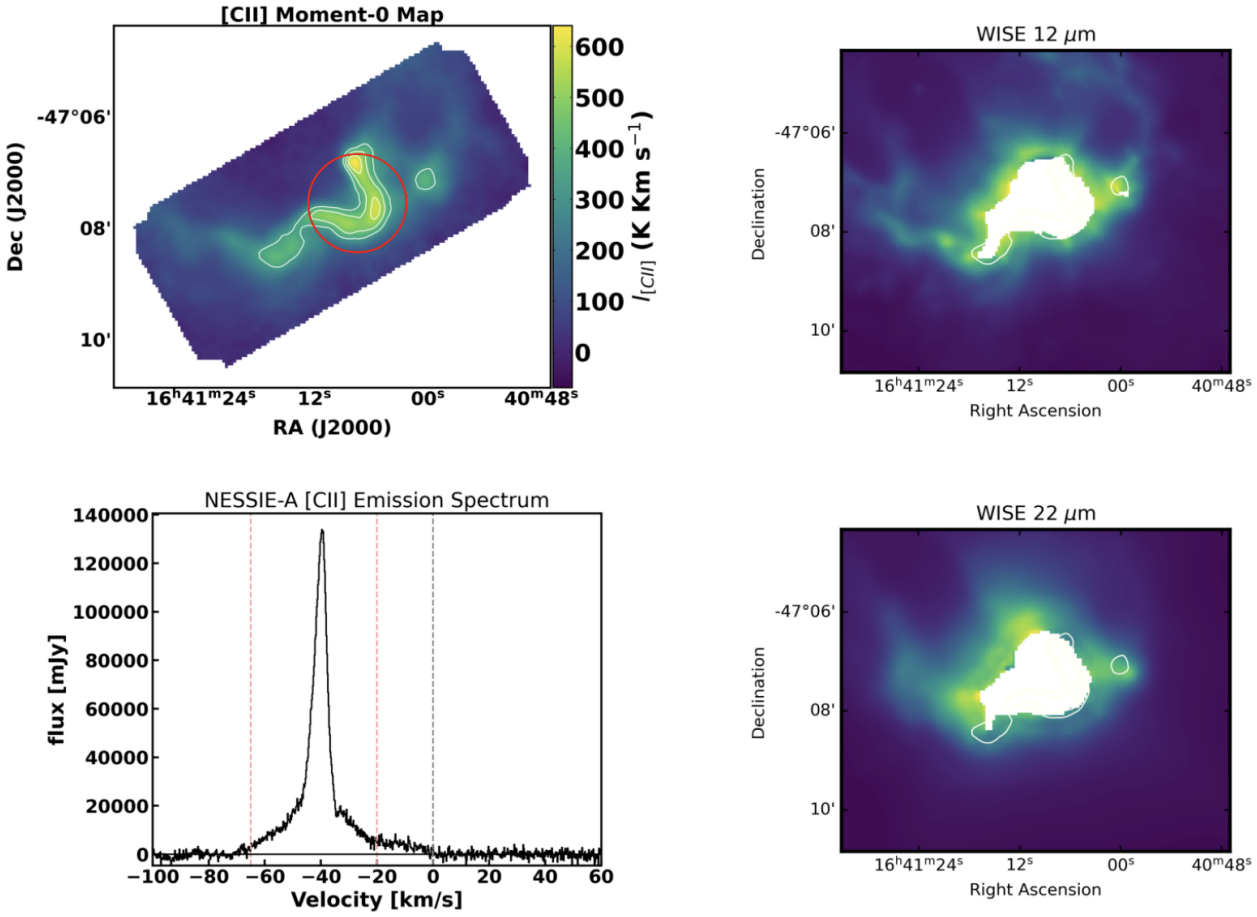

Figure 12. Top left: moment-0 map of SOFIA [C II] emission with 4, 5, 7, 9, 12, 15, and 18σ [C II] emission contours overlaid. The red circle indicates the sub-bubble NESSIE-Aa. Top right: WISE 12 μm emission (saturated) with [C II] contours overlaid. Bottom left: SOFIA [C II] spectrum of entire field. Bottom right: WISE 22 μm emission (saturated) with [C II] contours overlaid.

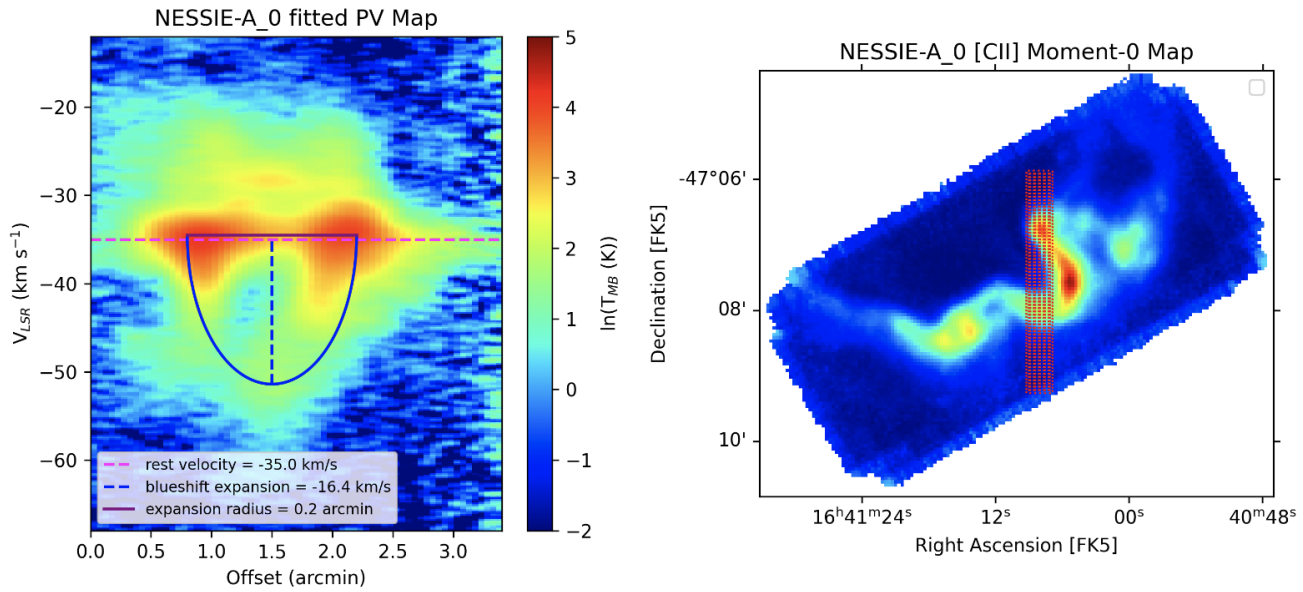

Figure 13. Left: PV diagram of the sub-bubble in NESSIE-A. Right: [C II] moment-0 map of NESSIE-A. The red area cutting across the field is the area from which the PV diagram on the left is derived.

of NESSIE-Aa to the main structure of NESSIE-A suggests potential interactions between the two, where the sub-bubble could be a site of new and ongoing triggered star formation, as suggested in J. M. Jackson et al. (2024).

7. Conclusion

We conducted a kinematic analysis of 35 H II regions mapped in [C II] 158 μm emission by SOFIA to investigate the expansion of their surrounding PDRs. Our key findings are summarized below:

1. *PV detection of expansion.* We use PV diagrams to identify expansion signatures in 12 of the 35 regions studied (∼34%). Most expansion appears blueshifted, while a smaller fraction shows redshifted or both blueshifted and redshifted. The average expansion velocity among our ECs is 12.21 km s^{-1}, supporting the idea that H II regions actively expand due to feedback from their ionizing stars.
2. *Regions without PV-detected expansion.* Of the 23 regions without detected expansion, all have radii smaller than their predicted stagnation radii (where F^* is available), suggesting they have not yet stagnated and are likely still expanding at undetectable or asymmetric rates.
3. *Velocity residual maps.* Velocity residual maps support the PV analysis and also allow us to examine deviations from homogeneous expansion. Only one of the 10 residual maps falls within the error bars of its corresponding PV diagram finding, while the others deviate by only a few kilometers per second but still yield consistent morphological fits. Simulations show that higher expansion velocities and S/N values yield more reliable expansion velocity fits.
4. *Expansion mechanisms.* Comparisons of observed expansion velocities with theoretical models suggest different driving mechanisms. Thermal pressure appears to dominate in M43, while stellar wind pressure is the likely driver in M17, M42, RCW 120, and RCW 79. The expansion in RCW 36 falls within both theoretical models, making it difficult to determine if one mechanism dominates over the other.
5. *Radial expansion asymmetry.* Some regions exhibit significant variations in expansion velocity along different axes, likely influenced by local density variations. Differences in blueshifted and redshifted expansion velocities may reflect foreground and background density differences.
6. *Dynamical ages versus stellar lifetimes.* Estimated dynamical ages of ECs are consistently an order of magnitude or more shorter than the main-sequence lifetimes of their ionizing sources. Possible explanations include delayed onset of expansion due to confinement by dense natal material, expansion into a clumpy or porous medium, and projection effects. High observed expansion velocities may also result from photoablation of molecular clouds along the ionization front.

The expansion and feedback of H II regions play a crucial role in shaping the ISM, regulating star formation rates, and influencing galactic evolution. Future studies of H II region expansion should focus on increasing the sample size, which will help refine our understanding of how H II regions evolve over time. More detailed constraints on ionizing sources will also help to disentangle the mechanisms driving expansion.

Acknowledgments

This study is based on observations made with the NASA/DLR Stratospheric Observatory for Infrared Astronomy (SOFIA). SOFIA is jointly operated by the Universities Space Research Association Inc. (USRA), under NASA contract NNA17BF53C, and the Deutsches SOFIA Institut (DSI), under DLR contract 50 OK 0901 to the University of Stuttgart. upGREAT is a development by the MPIfR and the KOSMA/Universität zu Köln, in cooperation with the DLR Institut für

Optische Sensorsysteme. T.F. and L.D.A. acknowledge support from Universities Space Research Association grant "H II Region Dynamics Revealed by [C II] Emission" #09-0520. N.S. acknowledges support (FEEDBACK-plus project) by the BMWI via DLR, Project Number 50OR2217. This work was supported by the CRC1601 (SFB 1601 sub-projects A6, B2) funded by the DFG (German Research Foundation) – 500700252. T.F. and L.D.A. would also like to thank Dr. James Jackson, the former director of the NSF Green Bank Observatory, and Dr. Robin JR Williams for helping with specific research questions.

ORCID iDs

T. Faerber https://orcid.org/0009-0003-2745-5849
L. D. Anderson https://orcid.org/0000-0001-8800-1793
M. Luisi https://orcid.org/0000-0001-8061-216X
L. Bonne https://orcid.org/0000-0002-0915-4853
N. Schneider https://orcid.org/0000-0003-3485-6678
V. Ossenkopf-Okada https://orcid.org/0000-0002-8351-3877
A. G. G. M. Tielens https://orcid.org/0000-0003-0306-0028
R. Simon https://orcid.org/0000-0003-2555-4408
M. Röllig https://orcid.org/0000-0001-6205-2242

References

Anderson, L., Makai, Z., Luisi, M., et al. 2019, ApJ, 882, 11
Anderson, L., Zavagno, A., Deharveng, L., et al. 2012, A&A, 542, A10
Anderson, L., Zavagno, A., Rodón, J., et al. 2010, A&A, 518, L99
Anderson, L. D., Bania, T., Balser, D. S., et al. 2014, ApJS, 212, 1
Balser, D. S., Goss, W., & De Pree, C. 2001, AJ, 121, 371
Bania, T., Balser, D. S., Rood, R. T., Wilson, T., & Wilson, T. 1997, ApJS, 113, 353
Barman, S., Neelamkodan, N., Madden, S. C., et al. 2022, ApJ, 930, 100
Belloni, T., & Mereghetti, S. 1994, A&A, 286, 935
Benaglia, P., Koribalski, B., Peri, C. S., et al. 2013, A&A, 559, A31
Bertoldi, F. 1989, ApJ, 346, 735
Beuther, H., Schneider, N., Simon, R., et al. 2022, A&A, 659, A77
Bisbas, T. G., Haworth, T., Williams, R., et al. 2015, MNRAS, 453, 1324
Bonne, L., Bontemps, S., Schneider, N., et al. 2023a, ApJ, 951, 39
Bonne, L., Kabanovic, S., Schneider, N., et al. 2023b, A&A, 679, L5
Bonne, L., Schneider, N., Garcìa, P., et al. 2022, ApJ, 935, 171
Cambrésy, L., Marton, G., Feher, O., Tóth, L. V., Schneider, N., et al. 2013, A&A, 557, A29
Carral, P., Kurtz, S. E., Rodríguez, L. F., et al. 2002, AJ, 123, 2574
Churchwell, E., Povich, M. S., Allen, D., et al. 2006, ApJ, 649, 759
Comerón, F., Djupvik, A., & Schneider, N. 2022, A&A, 665, A76
Dale, J., Haworth, T., & Bressert, E. 2015, MNRAS, 450, 1199
Damiani, F., Prisinzano, L., Micela, G., & Sciortino, S. 2019, A&A, 623, A25
Deharveng, L., & Zavagno, A. 2010, in IAU Symp. 270, Computational Star Formation, ed. J. Alves (Cambridge: Cambridge Univ. Press), 239
Draine, B. T. 2011, Physics of the Interstellar and Intergalactic Medium (Princeton, NJ: Princeton Univ. Press)
Ellerbroek, L., Bik, A., Kaper, L., et al. 2013, A&A, 558, A102
Elmegreen, B. G., & Lada, C. J. 1977, ApJ, 214, 725
Figueira, M., Zavagno, A., Deharveng, L., et al. 2017, A&A, 600, A93
Fleener, C. E., Payne, J. T., Chu, Y.-H., Chen, C.-H. R., & Gruendl, R. A. 2009, AJ, 139, 158
Franco, J., Kurtz, S., García-Segura, G., & Hofner, P. 2000, Ap&SS, 272, 169
Franco, J., Tenorio-Tagle, G., & Bodenheimer, P. 1989, in IAU Symp. 120, Structure and Dynamics of the Interstellar Medium, ed. G. Tenorio-Tagle (Cambridge: Cambridge Univ. Press), 96
Galván-Madrid, R., Peters, T., Keto, E. R., et al. 2011, MNRAS, 416, 1033
García-Rojas, J., Esteban, C., Peimbert, M., et al. 2006, MNRAS, 368, 253
Geist, E., Gallagher, J., Kotulla, R., et al. 2022, PASP, 134, 064301
Georgelin, Y., & Georgelin, Y. 1970, A&AS, 3, 1
Goodman, A. A., Alves, J., Beaumont, C. N., et al. 2014, ApJ, 797, 53
Graczyk, D., Pietrzyński, G., Thompson, I. B., et al. 2020, ApJ, 904, 13
Guevara, C., Stutzki, J., Ossenkopf-Okada, V., et al. 2020, A&A, 636, A16
Güsten, R., Heyminck, S., Wiesemeyer, H., et al. 2007, A&A, 454, L13
Hanson, M. M., & Conti, P. S. 1995, ApJL, 448, L45
Heyminck, S., Graf, U., Güsten, R., et al. 2012, A&A, 542, L1
Hollenbach, D. J., & Tielens, A. 1999, RvMP, 71, 173
Howarth, I. D., & Prinja, R. K. 1989, ApJ, 69, 527
Jackson, J. M., & Kraemer, K. E. 1999, ApJ, 512, 260
Jackson, J. M., Whitaker, J. S., Chambers, E., et al. 2024, ApJ, 965, 187
Jeffries, R. 2007, MNRAS, 376, 1109
Kabanovic, S., Schneider, N., Ossenkopf-Okada, V., et al. 2022, A&A, 659, A36
Karim, R. L., Pound, M. W., Tielens, A. G., et al. 2023, AJ, 166, 240
Karr, J., & Martin, P. 2003, ApJ, 595, 900
Keto, E. 2002, ApJ, 580, 980
Kirsanova, M., Sobolev, A., & Thomasson, M. 2017, ARep, 61, 760
Kirsanova, M. S., Ossenkopf-Okada, V., Anderson, L., et al. 2020, MNRAS, 497, 2651
Koo, B.-C. 1997, ApJS, 108, 489
Krabbe, A., Mehlert, D., Röser, H.-P., & Scorza, C. 2013, EJPh, 34, S161
Kuhn, M. A., Hillenbrand, L. A., Sills, A., Feigelson, E. D., & Getman, K. V. 2019, ApJ, 870, 32
Lacy, J., Richter, M., Greathouse, T., Jaffe, D., & Zhu, Q. 2002, PASP, 114, 153
Lancaster, L., Ostriker, E. C., Kim, C.-G., Kim, J.-G., & Bryan, G. L. 2024, ApJ, 970, 18
Lefloch, B., Lazareff, B., & Castets, A. 1997, in IAU Symp. 182, Herbig-Haro Flows and the Birth of Stars, ed. F. Malbet & A. Castets (Cambridge: Cambridge Univ. Press), 15
Lenz, D. D., & Ayres, T. R. 1992, PASP, 104, 1104
Lim, W., & De Buizer, J. M. 2019, ApJ, 873, 51
Lim, W., De Buizer, J. M., & Radomski, J. T. 2020, ApJ, 888, 98
Luisi, M., Anderson, L. D., Schneider, N., et al. 2021, SciA, 7, eabe9511
Luong, Q. N., Motte, F., Schuller, F., et al. 2011, A&A, 529, A41
Lynds, B. T., & Oneil, E. J., Jr 1985, ApJ, 294, 578
Martín-Hernández, N., Peeters, E., & Tielens, A. 2008, A&A, 489, 1189
Martins, F., Pomarès, M., Deharveng, L., Zavagno, A., & Bouret, J. 2010, A&A, 510, A32
Martins, F., Schaerer, D., & Hillier, D. J. 2005, A&A, 436, 1049
McBreen, B., Fazio, G., & Jaffe, D. 1982, ApJ, 254, 126
Moscadelli, L., & Goddi, C. 2014, A&A, 566, A150
Ochsendorf, B. B., Zinnecker, H., Nayak, O., et al. 2017, NatAs, 1, 784
Pabst, C., Goicoechea, J., Cuadrado, S., et al. 2024, A&A, 688, A7
Pabst, C., Goicoechea, J. R., Hacar, A., et al. 2022, A&A, 658, A98
Pabst, C., Goicoechea, J. R., Teyssier, D., et al. 2020, A&A, 639, A2
Pietrzyński, G., Graczyk, D., Gallenne, A., et al. 2019, Natur, 567, 200
Pomarès, M., Zavagno, A., Deharveng, L., et al. 2009, A&A, 494, 987
Povich, M. S., Stone, J. M., Churchwell, E., et al. 2007, ApJ, 660, 346
Raga, A. C., Cantó, J., Rodríguez, L. F., et al. 2012, RMxAA, 48, 149
Ragan, S. E., Henning, T., Tackenberg, J., et al. 2014, A&A, 568, A73
Reid, M., Menten, K., Brunthaler, A., et al. 2014, ApJ, 783, 130
Risacher, C., Güsten, R., Stutzki, J., et al. 2018, JAI, 7, 1840014
Rosen, A. L., Lopez, L. A., Krumholz, M. R., & Ramirez-Ruiz, E. 2014, MNRAS, 442, 2701
Roshi, D. A., Balser, D. S., Bania, T. M., Goss, W. M., & De Pree, C. 2005, ApJ, 625, 181
Russeil, D., Tigé, J., Adami, C., et al. 2016, A&A, 587, A135
Rygl, K., Brunthaler, A., Sanna, A., et al. 2012, A&A, 539, A79
Saha, A., Tej, A., Liu, H.-L., et al. 2024, ApJL, 970, L40
Sandell, G., Wright, M., Güsten, R., et al. 2020, ApJ, 904, 139
Schneider, N., Bonne, L., Bontemps, S., et al. 2023, NatAs, 7, 546
Schneider, N., Simon, R., Guevara, C., et al. 2020, PASP, 132, 104301
Schneider, N., Csengeri, T., Hennemann, M., et al. 2012, A&A, 540, L11
Shimoikura, T., Dobashi, K., Nakamura, F., Shimajiri, Y., & Sugitani, K. 2018, PASJ, 71, S4
Spitzer, L. 1968, Interscience Tracts on Physics and Astronomy, No. 28 (New York: Wiley)
Stacey, G., Townes, C., Poglitsch, A., et al. 1991, ApJL, 382, L37
Strömgren, B. 1939, ApJ, 89, 526
Tielens, A., & Hollenbach, D. 1985, ApJ, 291, 747
Tielens, A. G. G. M. 2005, The Physics and Chemistry of the Interstellar Medium (Cambridge: Cambridge Univ. Press)
Tiwari, M., Karim, R., Pound, M., et al. 2021, ApJ, 914, 117
Tiwari, M., Menten, K., Wyrowski, F., et al. 2019, A&A, 626, A28
Tothill, N. F., Gagné, M., Stecklum, B., & Kenworthy, M. A. 2008, in Handbook of Star Forming Regions, Volume II: The Southern Sky, ed. B. Reipurth, Vol. 5 (San Francisco, CA: ASP), 533
Townsley, L. K., Broos, P. S., Garmire, G. P., et al. 2014, ApJS, 213, 1
Townsley, L. K., Broos, P. S., Garmire, G. P., et al. 2018, ApJS, 235, 43

Townsley, L. K., Broos, P. S., Garmire, G. P., & Povich, M. S. 2019, ApJS, 244, 28
Treviño-Morales, S., Fuente, A., Sánchez-Monge, Á., et al. 2019, A&A, 629, A81
Verma, R., Bisht, R., Ghosh, S., et al. 1994, A&A, 284, 936
Walch, S., Whitworth, A., Bisbas, T., Hubber, D., Wünsch, R., et al. 2015, MNRAS, 452, 2794
Weaver, R., McCray, R., Castor, J., Shapiro, P., Moore, R., et al. 1977, ApJ, 218, 377
Wenger, T. V., Balser, D. S., Anderson, L., & Bania, T. 2018, ApJ, 856, 52
Werner, M., Becklin, E., Gatley, I., et al. 1979, MNRAS, 188, 463
Whitney, B., Indebetouw, R., Babler, B., et al. 2004, ApJS, 154, 315
Wolfire, M. G., Vallini, L., & Chevance, M. 2022, ARA&A, 60, 247
Xu, J.-L., Zavagno, A., Yu, N., et al. 2019, A&A, 627, A27
Xu, Y., Moscadelli, L., Reid, M., et al. 2011, ApJ, 733, 25
Zamora-Avilés, M., Vázquez-Semadeni, E., González, R. F., et al. 2019, MNRAS, 487, 2200
Zavagno, A., Deharveng, L., Comerón, F., et al. 2006, A&A, 446, 171
Zavagno, A., Russeil, D., Motte, F., et al. 2010, A&A, 518, L81
Zhu, Q.-F., Lacy, J. H., Jaffe, D. T., Richter, M. J., & Greathouse, T. K. 2005, ApJ, 631, 381